ACS APPLIED NANO MATERIALS

www.acsanm.org
Article

Robust Basal-Plane Functionalization with Masked *N*-Heterocyclic Carbenes Gives Semiconducting MoS_2 and WS_2 Nanoflakes

Quoc Minh Tran, Yunsoo Choi, Nikolaos Chalmpes, Drake Austin, Supawitch Hoijang, Melissa Ariza Gonzalez, Minh Dang Nguyen, Pailinrut Chinwangso, Viktor G. Hadjiev, Arnold M. Guloy, Allan J. Jacobson, Nicholas R. Glavin, Richard A. Vaia,* and T. Randall Lee*

Cite This: *ACS Appl. Nano Mater.* 2025, 8, 22400−22417

ABSTRACT: Tailoring the surface characteristics of layered transition metal dichalcogenides (LTMDs) is critical for optimizing performance for integration into advanced technological devices. Group VI LTMDs offer exceptional potential in fields such as optoelectronics, energy storage, and sensing. However, their fully occupied valence band poses challenges in establishing strong interfacial interactions and facilitating composite formation. Herein, we report a strategy for basal-plane functionalization of Group VI LTMDs using masked *N*-heterocyclic carbenes (NHCs). As mild nucleophiles, NHCs facilitate electron transfer into the unoccupied conduction band while preserving structural integrity and the semiconducting properties of the LTMDs such as MoS_2 and WS_2. The elevated electron density enables the functionalization and the formation of a bilayer self-assembled monolayers of NHC precursors on the surface of the few-to-monolayer LTMDs through ionic interactions, leading to restacked superlattice structures. Notably, the masked NHC layers effectively suppress interlayer coupling, thereby maintaining the monolayer-like semiconducting behavior in the restacked materials. The robust interactions between masked NHCs and LTMDs, along with retention of semiconducting properties, is demonstrated in detail. These findings introduce a versatile method for surface modifications of LTMDs and establish a synthetic pathway to an emerging class of materials. This approach expands the functional applicability of LTMDs across diverse technological platforms.

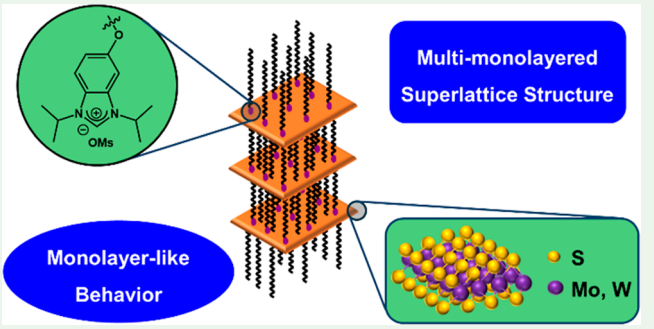

KEYWORDS: *N-heterocyclic carbenes, self-assembled monolayers, transition metal dichalcogenides, MoS_2, WS_2, semiconductor, optoelectronics, surface functionalization*

INTRODUCTION

Few-to-monolayer solution dispersions of two-dimensional (2D) layered transition metal dichalcogenides (LTMDs) are emerging as cost-effective and scalable materials for potential integration into advanced technologies. These applications encompass energy generation and storage, field-effect transistors, memristors, optoelectronic devices, sensors, and filters, among others. The majority of studies have focused Group VI LTMDs (e.g., MoS_2 and WS_2), primarily owing to their exceptional stability and attractive semiconducting properties, particularly at monolayer architectures.[1] However, a persistent challenge lies in the limited availability of strategies to tailor the interfacial properties of these solution-processed 2D materials, thereby constraining the engineering of their optoelectronic properties.

To date, the reports on LTMDs surface-ligand configuration can be summarized into four distinctive types: chemical passivation of chalcogen defects,[2] edge-site covalent linkages,[3] physisorption,[4] and surface functionalization. While both chalcogen defects and edge-site covalent linkages involve the formation of unsaturated bonds, physisorption primarily coats the surface through weak, noncovalent interactions, without any robust chemical bonding. Surface functionalization, which entails direct covalency with the crystallographic basal plane of LTMDs, has been rarely reported, due to the inertness of the basal surface. This chemical inertness is particularly pronounced in semiconducting Group VI LTMDs, attributed to the fully occupied valence band electrons.

The exfoliation techniques employed to achieve exfoliated dispersions play a critical role in defining the initial characteristics and the corresponding implementation of surface hybridization strategies. For example, lithium intercalation—a

Received: September 22, 2025
Revised: October 13, 2025
Accepted: October 14, 2025
Published: November 7, 2025

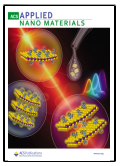

widely used exfoliation approach—activates the basal plane of LTMDs. The underlying driving mechanism is the potent electron transfer from alkali metals to the conduction bands, which are primarily composed of the d orbitals of transition metals. This electron transfer induces a crystallographic transformation from the thermodynamically stable semiconducting 2H phase to metastable metallic 1T phase.[5] The metastable 1T phase, characterized by its high electron density, can react with electrophilic species such as organohalides,[6] and epoxides,[7] or radical-initiated species such as diazonium salts,[8] and alkyl azide.[9] Despite that, the 1T phase loses the semiconducting characteristics while an additional phase transition to the 2H phase—typically induced by thermal treatment—might generate defects and chemical transformation. Common exfoliation methods to produce semiconducting few-to-monolayer dispersions typically rely on surface-solvent compatibility, requiring aqueous surfactant in water (H_2O), H_2O/isopropyl alcohol (IPA) mixtures,[11] or *N*-methyl-2-pyrrolidone.[12] Within these media, surface functionalization is restricted to thiol-based ligands via coupling chemistry, which forms weak S−S bonds and subsequently yields physisorbed dithiol molecules.[13] Consequently, these ligands behave as noninteracting surfactants, where both their molar ratio and surface/solvent matching energy play critical roles in maintaining colloidal stability. Furthermore, it has been reported that H_2O acts as a mild oxidant, inducing oxidative decomposition of LTMDs.[14] Recently, a novel exfoliation strategy based on redox chemistry has been introduced, enabling the efficient production of semiconducting 2H few-to-monolayer Group VI LTMD dispersions. This approach not only yields high-quality and large-area flakes (μm scale), but also expands the spectrum of compatible solvents, thereby overcoming the constraints associated with colloidal stability in specific solvent environments.[15,16] This advancement facilitates the exploration of alternative functionalization strategies employing organic species, particularly those with high solubility in organic protic/aprotic solvents. For instance, a mild covalent functionalization approach based on the Michael addition reaction has been recently proposed in acetonitrile solvent.[17] While this method offers a direct covalent toolbox—exploiting the mild nucleophilicity of semiconducting Group VI LTMDs, the degree of functionalization was overestimated due to subsequent polymerization.[18] Additionally, based on this analogy, it is reasonable to hypothesize that other electrophilic species, such as organohalides, could elicit comparable functionalization outcomes on 2H Group VI LTMDs. However, literature evidence suggests that, in the 2H phase, basal-plane functionalization has only been achieved in the presence of Pt^0 catalysts.[19]

From these observations, existing strategies can be summarized as follows: (1) mildly electrophilic species such as maleimides offer promise, albeit with limited versatility; (2) weak nucleophiles, including thiol-based molecules, predominantly interact via physisorption; and (3) strongly nucleophilic reagents, such as butyl lithium, tend to induce structural transformation rather than stable functionalization. Herein, it is important to note that any significant electron transfer, whether being injection or withdrawal, can provoke electronic and crystallographic changes that are thermodynamically unfavorable. This underscores a critical gap in functionalization approaches: the need for mild nucleophiles capable of donating minimal electron density, sufficient to establish robust interactions (covalent or ionic) while preserving the crystallographic integrity of the semiconducting 2H phase. Recent findings lend support to this hypothesis. For instance, MoS_2 partially reduced by $NaBH_4$ retains its semiconducting nature.[20] Complementarily, Duan and co-workers showed that molecular cations can be intercalated into the interlayer galleries of into single-crystal Group VI LTMDs (MoS_2, WSe_2) via an electrochemically driven anode-based method.[21] This approach facilitates electron doping, wherein the doping level can be modulated through steric hindrance imposed by the molecular cations, thereby maintaining the semiconducting nature of Group VI LTMDs. Supporting this concept, Vaia and colleagues highlighted the applicability of Lewis acid−base interactions: metallic Group V LTMDs function as Lewis acids, while amine or phosphine ligands serve as Lewis bases. Their findings indicate that such functionalization can yield semiconducting behavior (e.g., excitonic transitions) on otherwise metallic LTMD substrates.[22] This body of evidence collectively underscores the emerging potential of employing mild electrophiles to functionalize the basal plane of semiconducting Group VI LTMDs. The proposed strategies to date are summarized in Scheme 1. Building upon these insights, we propose that

Scheme 1. Group VI LTMD-Ligand Interactions Depending on the Reducing Strength of Organic Ligands

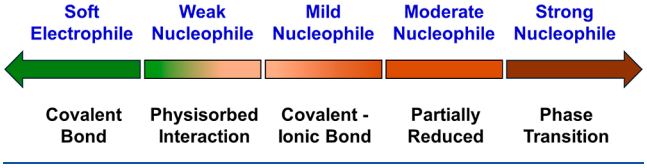

electron transfer from the ligands to the unoccupied conduction bands of semiconducting Group VI LTMDs could be facilitated by a carefully chosen reducing agent. Such an agent must be potent to promote bond formation, yet not so aggressive as to induce undesired phase transition—unlike butyl lithium. Conversely, excessively weak reducing agents lead to mere physisorption, as observed with dithiol-based ligands.

To address the need for generating robust surfaces, we report a Group VI semiconducting LTMD-organic ligand functionalization strategy that enables the direct functionalization of the basal plane of LTMDs (MoS_2, WS_2). As such, we chose *N*-heterocyclic carbenes (NHCs) in the form of benzimidazolium salts, owing to their mild electron-donating nature, as a proof-of-concept system. Surprisingly, during our manuscript submission, similar idea was also being demonstrated by Hersam's group on monolayer WS_2.[23] For our study, the adopted molecule, labeled as NHC15OH[OMs], was chosen based on our previously reported functionalization of gold surfaces (Figure 1).[24] To avoid the oxidative degradation induced by H_2O, the exfoliated few-to-monolayer LTMDs were produced under anhydrous conditions. Furthermore, we demonstrate that the surface functionalization is compatible with multiple exfoliated LTMD dispersions, prepared through different methods, including redox exfoliation and bath sonication.[15,16] Group VI LTMD dispersions stoichiometrically react with masked NHCs, forming bilayer self-assembled monolayers (SAMs) on the surface of the exfoliated 2D flakes through ionic interactions. Consequently, this robust surface functionalization alters the surface energy of the exfoliated 2D flakes, giving to a restacking phenomenon and the formation of superstructures. The resulting hybrids are stable and due to the electron donation to the surface, display a shifted optical response while preserving

https://doi.org/10.1021/acsanm.5c04402
ACS Appl. Nano Mater. 2025, 8, 22400−22417

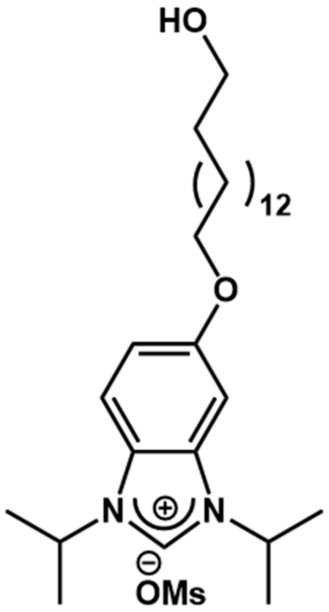

Figure 1. Molecular structure of NHC15OH[OMs].

the semiconducting behavior of monolayer LTMDs. These findings not only provide a synthetic framework to prepare a new class of LTMD-organic hybrids, but also insights into the electronic covalency nature of LTMDs and their potential tunability for functional applicability across advanced technological platforms.

RESULTS AND DISCUSSION

Exfoliated LTMD Dispersions—Heterogeneity Challenges. Few-to-monolayer dispersions were prepared by the redox exfoliation method (MoS_2, WS_2) and the liquid phase sonication method.[15,16,25] First, it is important to emphasize that both the exfoliation methods and the nature of the starting materials influence the initial physical and chemical characteristics of the resulting exfoliated dispersions.[26] To address this point, two different LTMD powders and exfoliation techniques were used. For the dispersions exfoliated using the redox exfoliation technique, commercial LTMD powders with grain boundaries <2 μm were employed. In contrast, for the dispersions exfoliated using the bath sonication technique, MoS_2 powder synthesized via a traditional two-step chemical vapor transport (CVT) method was employed.[25] For simplification, LTMDs exfoliated using the redox method are hereafter referred as "redox MoS_2" or "redox WS_2", while MoS_2 exfoliated via sonication are denoted as "CVT MoS_2". Second, all solution-based exfoliation methods inherently produce heterogeneous dispersions. This limitation poses a persistent challenge, impeding comprehensive insights into basal plane-functionalized systems, which will be discussed in detail in the next section.

The primary challenge associated with exfoliated dispersions is heterogeneity, which exhibits variability across batches. The term "heterogeneity" refers to the variations in the three-dimensional features of a 2D flake, including its shape (generalized by lateral length and width) as well as its thickness. Figure 2 demonstrates the heterogeneity of redox MoS_2 as resolved through fractionation via the centrifuge cascade technique (see Supporting Information, Size-Selection by Centrifuge Cascade, Scheme S1). The four dispersions, labeled as MoS_2 F1, F2, F3, and F4, were collected at centrifuge rates of 2000−2500 rpm, 2500−3000 rpm, 3000−4000 rpm, and >4000 rpm, respectively. Extinction (ε) spectra of these four dispersions, normalized at ε_{345}, are presented in Figure 2a, while the corresponding second derivatives are displayed in Figure 2b,d, respectively. Note that the extinction spectra encompass contribution from both absorbance (α) and size-dependent scattering (σ) background; hence, to enable meaningful comparisons among dispersions, the local minimum ε_{345}—an independent metric free from the influence of scattering effects—serves as a reference point for subsequent evaluations.[27] Additionally, within the range below 700 nm, the dominance of scattering background necessitates the conversion of the original extinction spectrum into its second derivatives. This mathematical transformation was essential to accurately deduce the excitonic peak positions from the broad scattering background. Within the spectral range of 700 to 350 nm, the excitonic peaks of MoS_2 were designated as A, B, C, and D. The wavelength positions corresponding to the A- and D-peaks, which have been proposed as reliable factors for estimating the mean thickness and lateral dimensions of the flake population, are summarized in Figure 2c.[27] As the centrifuge rates increased, the overall extinction spectra of collected dispersions displayed variations in signal intensity and blue shifts across all excitonic transitions, indicative of a reduction in flake size distribution.[28] This trend arises because centrifugation influences material separation based on differences in material mass. Although the dispersions obtained at high centrifuge rates are typically enriched with a higher proportion of monolayers, it is crucial to highlight that the population of a specific dispersion also includes small few-layer flakes, with variations in shape and dimensions.[27]

Given the inherent heterogeneity present in all dispersions, it is important to recognize that the parameters derived from extinction spectra correspond to the median flake population, rather than to flakes with well-defined size and thickness. Therefore, statistic studies on flake size and thickness were subsequently performed via scanning electron microscopy (SEM) and atomic force microscopy (AFM), respectively. In Figure 2e,f, SEM images, along with the subsequent statistical analyses, revealed that despite fractionation, the dispersions exhibited broad size distributions, as characterized by the lateral length and width of the 2D flakes. This size heterogeneity was further corroborated by the observed blue shift in excitonic peaks across the extinction spectra of all four fractions. The thickness heterogeneity was assessed using AFM, as summarized in Figure 3, where MoS_2 F1 and F4 were chosen to highlight the variations in thickness distribution, while analogous measurements were performed on unfractionated redox MoS_2, as depicted in Figure S1. Despite the relatively broad median thickness distributions of both MoS_2 F1 and F4 flakes—13.3 ± 9.0 nm and 2.2 ± 2.5 nm, respectively, in comparison to the commonly accepted monolayer thickness of 0.65 nm—we emphasize that each dispersion contains fractions of monolayer flakes, with the MoS_2 F4 dispersion being particularly enriched in monolayers. This assessment is based on the fact that liquid dispersions involve multiple species including exfoliated materials. This complexity leads to residue formation on the surface of 2D flakes, such as absorbed POMs, solvents, and surfactants.[10,15,16,27] To address this issue, an internal reference, known as "step height", was used, which was based on the observation that incomplete exfoliation gave to staircase-like height profile. In our analysis, a step height of approximately 2.0

https://doi.org/10.1021/acsanm.5c04402
ACS Appl. Nano Mater. 2025, 8, 22400−22417

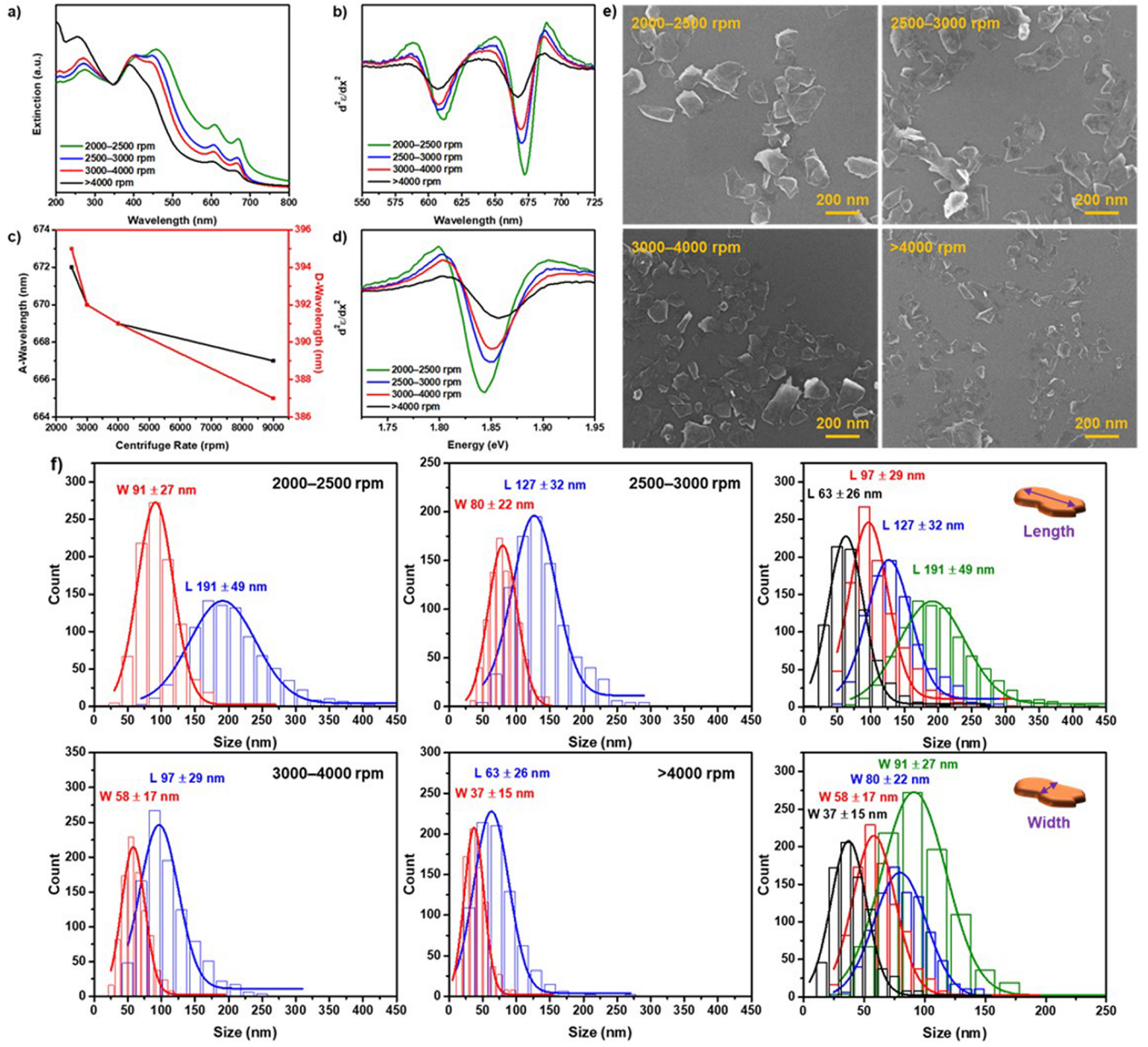

Figure 2. (a) Normalized extinction spectra, (b,d) the corresponding 2nd derivatives in the A−B-excitonic regions and A excitonic energy (eV), (c) A−D excitonic wavelengths of four fractional redox MoS_2 dispersions obtained at centrifuge rates of 2000−2500 rpm (MoS_2 F1), 2500−3000 rpm (MoS_2 F2), 3000−4000 rpm (MoS_2 F3), and >4000 rpm (MoS_2 F4). (e) SEM images, and (f) statistical size distribution of MoS_2 flakes for four fractional redox dispersions. Note that, in (f), the first four plots (left) represent the size distribution (L—lateral length and W—width) of individual fractions, while the last two figures (right) provide a comparative summary of either lateral length or width distributions across four fractions. The color scheme used in the plots correspond to that in Figure 1a to facilitate visual correlation between data sets.

to 3.0 nm was found and attributed to the thickness of a single layer (Figure S1). The height profile analysis of over 300 exfoliated MoS_2 flakes in unfractionated dispersion showed that the average thickness distribution is 9.7 ± 4.2 nm, corresponding to approximately 5 layers. Validation to the probed species, being indeed exfoliated materials, was double-checked by transmission electron microscopy (TEM). Detailed procedures for sample preparation for AFM measurements are provided in the Supporting Information (Thin-Film Fabrication, Scheme S2 and Characterization Notes). Powder X-ray diffraction (PXRD) was carried out to compare the structural characteristics of bulk and thin films of exfoliated MoS_2. The (00l) reflections, attributed to the interlayer correlations, remained due to restacking. Nevertheless, the ($h0l$) reflections, despite being significantly attenuated, remained detectable in trace amounts, indicating the presence of few-layered MoS_2 (Figure S1). Similar observations were observed in the case of redox WS_2 dispersions, as depicted in Figures S2−S4.

In addition to variations in size and thickness, the surface properties of exfoliated dispersions also underwent alteration to some extent, either as an interdependent factor influenced by flake size or as a consequence of the specific exfoliation methods utilized. For example, the surface Zeta potentials of redox and CVT MoS_2 dispersions showed a comparable disparity, which can be attributed to their respective dispersion mechanisms. Redox MoS_2 is stabilized via surface adsorbed inorganic polyoxometalates (POMs), whereas CVT MoS_2 achieves dispersion via a surface/solvent matching mechanism. The

https://doi.org/10.1021/acsanm.5c04402
ACS Appl. Nano Mater. 2025, 8, 22400−22417

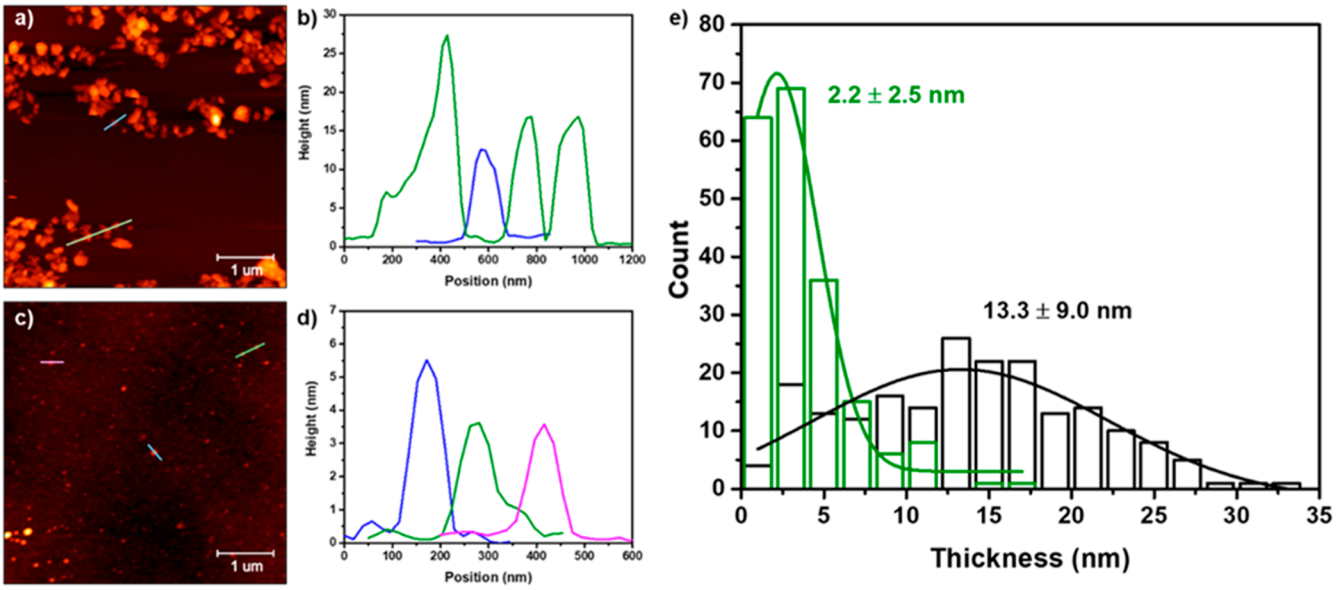

Figure 3. AFM images and the corresponding height profiles of selected flakes of redox MoS_2 F1 (a,b) and F4 (c,d). (e) Thickness distribution of redox MoS_2 F1 (black) and F4 (green), the counted population for each dispersion is $N = 200$ flakes.

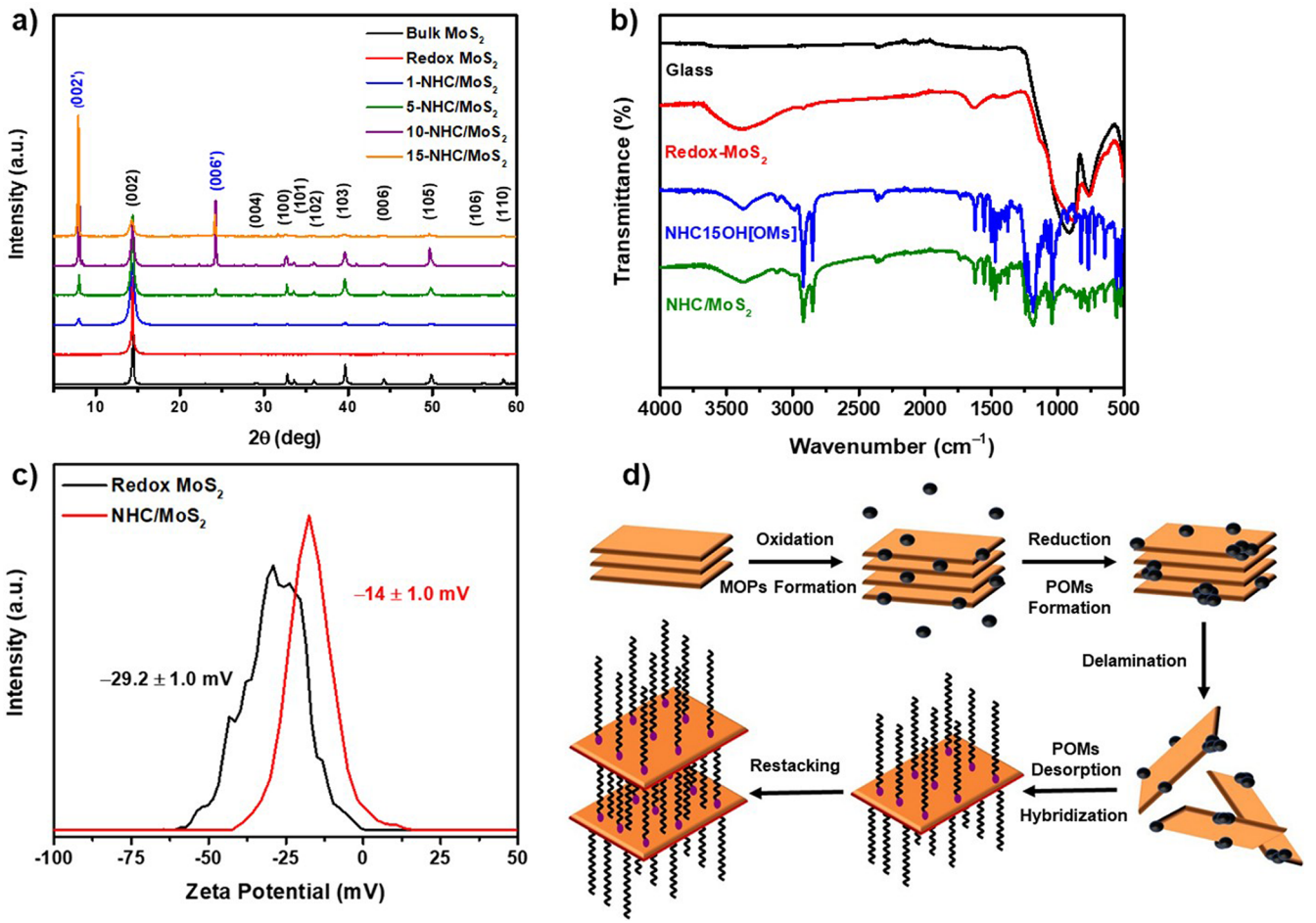

Figure 4. (a) PXRD patterns, (b) ATIR spectra, (c) Zeta potential of NHC-functionalized MoS_2, labeled as x-NHC/MoS_2 where x represents the NHC/MoS_2 molar ratio, and (d) the proposed interaction scheme involves the following steps: (1) exfoliation of MoS_2 nanoflakes via redox exfoliation, leading to surface adsorption of POMs; (2) exposure to masked NHCs, inducing desorption of POMs and subsequent surface hybridization; and (3) agglomeration and self-restacking of the functionalized nanoflakes, leading to the formation of intercalated superlattice structures.

https://doi.org/10.1021/acsanm.5c04402
ACS Appl. Nano Mater. 2025, 8, 22400−22417

Scheme 2. Two Intercalated Structures Arise from the Restacking of Functionalized LTMDs

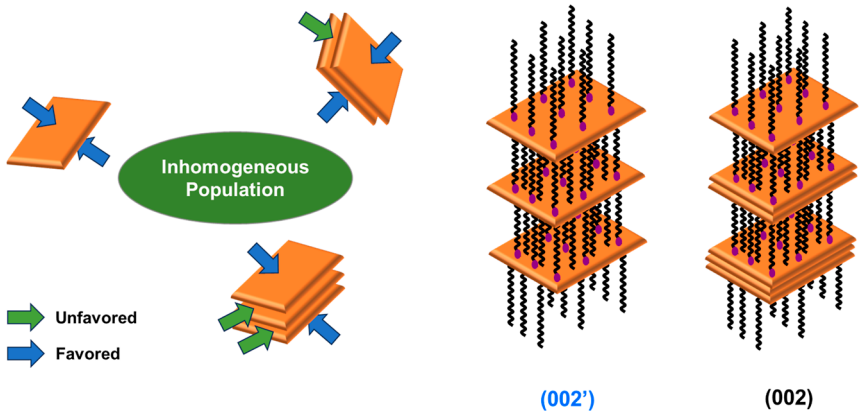

adsorption of POMs onto the layer leads to more negative Zeta potential in redox MoS_2 dispersions (−29.2 mV) compared to CVT MoS_2 dispersions (−15.6 mV). Furthermore, the concentration of adsorbed POMs might vary depending on the surface area of the 2D LTMD flakes and the specific reducing agents used during the redox exfoliation process (Figure S5). This surface heterogeneity serves as an important consideration since the adsorbed POMs have been reported to potentially function as dopants, thereby impacting the optical properties of Group VI LTMDs.[26] These effects, attributable to the dielectric modifications, have been documented elsewhere.[29]

Surface Hybridization: NHC-Functionalized Few-To-Monolayer LTMDs. The concentration of exfoliated MoS_2 (and WS_2) within the as-prepared dispersion was systematically determined through extrapolation, followed by a titration procedure (Figures S6 and S7). Exfoliated LTMD dispersions in anhydrous acetonitrile (a-ACN) were introduced into a solution of NHC15OH[OMs] in dichloromethane (DCM). Rapid compression and subsequent agglomeration could be observed within minutes, leading to the formation of swollen, intercalated materials. Figure 4a summarizes PXRD patterns of collected and washed powders of the hybridized products for reactions at increasing molar ratio of masked NHCs to redox MoS_2 (1:1 to 1:15). The diffraction patterns reveal two distinct and prominent peaks at 7.98 and 24.25 (2θ), attributable to a molecular environment between MoS_2 single layers. The interlayer gallery expands by 5.0 Å for an interlayer spacing of 11.1 Å (7.98 2θ). We then reviewed previous reports deducing the molecular orientation and packing arrangements of NHCs within the gallery (Supplementary Note 1, Figures S8 and S9). The resulting intercalated structure is composed of NHC ligands lying flat on the LTMD surfaces and extending from both sides of the 2D flakes. Note that, if the edge site or defect functionalization dominated, no substantial increase in the gallery would occur, and the interlayer spacing would remain unchanged. Due to the interlayer organic species, off-axis reflections—such as $\{hkl\}$, $\{h0l\}$, and $\{0kl\}$, which represent the crystallographic lateral registry between layers—are unexpected in the intercalated structure. However, reflections along c-axis $\{00l\}$ and within $a-b$ plane $\{hk0\}$ are anticipated, consistent with the emergence of new $(00l')$ reflections, and the retention of (100) and (110) reflections in both the hybrid and MoS_2. In contrast, unexpected (101), (102), (103), and (105) reflections are significantly suppressed in the hybridized materials; their weak intensity is indicative of a fraction of unfunctionalized MoS_2 in the intercalated product, as also indicated by the (002) and (004) reflections of MoS_2.

To offer complementary evidence of interlayer entrapped NHCs, attenuated total reflectance infrared (ATIR) spectra of the washed 15-NHC/MoS_2 hybrid showed the presence of NHC15OH[OMs] as illustrated in Figure 4b. IR has been reported as a reliable technique to provide direct information about the organic structures of intercalated species.[30] Studies have shown that the frequency, width, height, and integrated intensity of the CH_2 and CH_3 infrared absorption bands are sensitive to the gauche/trans conformer ratio of the hydrocarbon chains, as well as to the intermolecular interactions occurring between the chains.[30] In our study, the bands at 2919.9 and 2850.0 cm^{-1} arise from the asymmetric $\nu_{as}^{(CH_2)}$ and symmetric $\nu_{s}^{(CH_2)}$ stretch, respectively. These bands were consistently present in both solid NHC15OH[OMs] powder and the intercalated 15-NHC/MoS_2 hybrid powder, indicating similar structural features. This observation indicates an organic layer crystallized within the galleries of the MoS_2 framework, which is consistent with the PXRD patterns of NHC15OH-[OMs] powder and the NHC/MoS_2 hybrid (Figure S10).

In addition to the structural change within the galleries, the surface texture of the layers is altered. Prior to functionalization, the surface properties of redox MoS_2 are dominated by the POM adsorbates. Following functionalization, these negatively charged adsorbates are absent and replaced with organic species on the MoS_2 layers, which is indicated by a positive Zeta potential shift (Figure 4c). This shift is comparable to that observed in exfoliated MoS_2 produced via bath sonication in the absence of surface-adsorbed POMs (Figure S11). Desorption of the POMs was accompanied by restacking of the MoS_2 (and WS_2) flakes, highlighting the critical role of POMs and NHCs in modulating surface energy, either maintaining a stable dispersion state or leading to an agglomerated powder state.[31] However, evaluation of complete POM desorption is challenging due to the complex variable stoichiometry of POMs during their formation, as well as potential misidentification of POMs with oxidized Mo species localized at flake edge sites—a consequence of redox-driven exfoliation process.[15,26] The proposed scheme for the functionalization process, which gives rise to the formation of a restacked superlattice structure, is illustrated in Figure 4d.

As demonstrated, the heterogeneity and intrinsic characteristics of as-prepared LTMD dispersions, stemming from fractionation and exfoliation methods utilized, are unavoidable. Given these challenges, we discuss below that, despite being

https://doi.org/10.1021/acsanm.5c04402
ACS Appl. Nano Mater. 2025, 8, 22400−22417

interdependent, collective factors can be tentatively decoupled and analyzed to provide deeper insights into the hybrid system.

Effects of Reactant Concentration. At a low synthetic ratio (NHC/MoS_2, 1:1), the gallery expands to an interlayer spacing of 11.1 Å, a value comparable to that observed under oversaturation conditions at higher synthetic ratios of 10:1 or 15:1. This behavior indicates the gallery being influenced by a nongoverned kinetic mechanism, particularly in the case of redox-exfoliated LTMDs. It is critical to note that even though an increase in synthetic ratio demonstrates a greater quantity of intercalated products, a trace amount of few-layered MoS_2 persists. On the other hand, the intensity of the characteristic peak corresponding to the intercalated hybrids might exhibit batch-by-batch variability. Since the initial MoS_2 dispersion is composed of both single-layer and few-layer flakes, the experimental data imply that the masked NHCs primarily react on the outer surface of layers, without penetrating and disrupting between the layers of few-layer stacks (Scheme 2). These observations also indicate that thermodynamic driving forces for the reaction are insufficient to overcome the additional entropic penalty of interlayer confinement. To rule out the possibility that destabilization caused by introduced masked NHCs led to quick agglomeration and restacking, a control experiment was set up, using sonication to redisperse the materials, thereby allowing more time for the reaction to proceed (Figure S10). The data confirmed that a complete intercalated state was not attainable, and the final superstructure hybrid is a product of surface functionalization rather than intercalation. Interestingly, PXRD patterns of the sonicated samples exhibit the emergence of a unique peak at 6.77 (2θ), corresponding to an interlayer spacing of 13.0 Å, labeled as (002*). This new reflection is indicative of structural disorder introduced by successive disturbances due to sonication, while the (002′) reflection remains prominent (Figure S10).

Herein, we emphasize that both surface functionalization and intercalation lead to formation of the final intercalated state; however, these two processes are mechanistically distinct to a certain extent. Intercalation refers to the process by which guest species penetrate and reside within the interlayer galleries of multilayer LTMDs. This process typically requires the guest species to be sufficiently small—such as in the case of Li cations—and a fully intercalated state is generally achievable. Larger species—such as molecular cations—required an external input of energy, such as an applied voltage, to overcome the interlayer attraction and the restricted interlayer spacing of multilayer LTMDs. To date, direct intercalation, except Li cations, into multilayered Group VI LTMDs remains a significant challenge and has not been demonstrated. In contrast, surface functionalization refers exclusively to the interactions on the surface. The functionalizing species do not infiltrate and occupy the interlayer galleries of multilayer LTMDs. When the exfoliated dispersions contain a sufficiently high proportion of monolayer flakes, the colloidal stability is reduced causing aggregation, re-stacking of the layers with the surface attached molecular species, and the production of an intercalated (hybrid layered) structure. Conversely, when the exfoliated dispersions are dominated by few-layered flakes, or when the formation of densely packed SAMs on the basal plane is not achieved, such intercalated architectures are not observed.[18,22] In addition, the surface interactions might encompass not only covalent bonds[6] but also extend to physisorption and ionic bonds.[32]

To optimize both the quality and quantity of the intercalated product, it is evident that a high concentration of single layer material is needed, such MoS_2 F4 (Figure S10). In contrast, a dispersion containing a mixture of mono- to few-layered LTMD flakes will lead to the formation of two coexisting structures (Scheme 2). (Note: The intercalated structures, depicted in Figure 4, Scheme 2, and other related figures, are intended for illustrative purposes only. As discussed, the functionalizing species lie flatly on the nanoflake surfaces with the alkyl chains oriented either parallel to the surface or with a slight tilt rather than adopting a perpendicular, upright configuration. Additionally, the alkyl tails can adopt any conformations (gauche, trans) and orientation depending on the area per headgroup, which will be discussed in the next section.) While the first structure (left) contributes to the (002′) or (002*) reflections, the second structure (outer right), solely contributes to the (002) reflections, resembling the behavior observed in multilayered LTMDs. Importantly, the intensity of (002′) and (002*) reflections, in dispersions with a high concentration of few-layered LTMDs, might vary due to the inherently random and uncontrollable stacking manner of these mono- and few-layered species. Similar observations were conducted in the case of 15-NHC/WS_2 hybrid (Figure S10).

Effects of Flake Size. The impact of flake size on the molecular environment was investigated through the functionalization of redox MoS_2 fractional dispersions with masked NHCs. Upon size selection, two distinct intercalated phases, (002′) and (002*), became evident and significant. Dispersions enriched with smaller flakes, such as MoS_2 F3 and F4, predominantly exhibited a larger interlayer spacing of 13.0 Å. Meanwhile, MoS_2 F1 and F2, which are composed of larger flakes, typically gave a smaller interlayer spacing of 11.1 Å. Even so, it is noteworthy that an interlayer spacing of 13.0 Å is occasionally observed in MoS_2 F1 and F2. In contrast, unfractionated redox MoS_2 dispersions consistently showed a single gallery of 11.1 Å, with negligible phase transition from (002′) to (002*) upon external disturbance, such as sonication. The observed increase in interlayer gallery of 1.9 Å illustrates that the organic environment within the interlayer galleries display structural variations in intercalated hybrids produced from different dispersions.

When molecules form SAMs on two sides of flakes, two key factors should be considered: (1) molecular coverage, which is influenced by the steric hindrance of the molecules and the surface area of the flakes; and (2) intermolecular interactions, primarily governed by van der Waals (vdW) forces arising from the long hydrocarbon chains. Consequently, to optimize the packing density of molecules within the LTMD interlayer galleries across different fractions with varying flake areas, molecules tend to adopt specific orientations. These might include fully extended trans conformations or gauche conformations of the hydrocarbon chains, depending on the spatial constraints and the nature of intermolecular interactions. However, the molecular packing density, packing ordering, and orientation—collectively referred as the molecular environment—are difficult to resolve using PXRD, which principally provides information on interlayer spacing. Notably, intercalated structures exhibiting similar comparable interlayer spacings might still possess distinct molecular environments that remain undetectable solely by PXRD. This limitation was commonly encountered in previous reports for intercalated structures involving various layered host frameworks, such as layered silicates. An indirect method to assess such complex

https://doi.org/10.1021/acsanm.5c04402
ACS Appl. Nano Mater. 2025, 8, 22400−22417

molecular environments is the employment of IR spectroscopy to analyze the vibrational mode of the CH_2 groups.[30] The band at around 2920 cm^{-1} arise from the asymmetric $\nu_{as}^{(CH_2)}$ stretch, which can be used as a comparative metric to analyze the packing density as well as the gauche/trans conformer ratio of the methylene chain. In general, a shift of the $\nu_{as}^{(CH_2)}$ vibration to lower wavenumbers indicates an increase in interlayer packing density, accompanied by a greater adoption of trans conformations by the alkyl chains. Correspondingly, the phase state of the organic interlayer can be determined, with a greater solid-like nature (trans conformations) corresponding to order, or more liquid-like state (gauche conformations) associated with increased disorder. Herein, the asymmetric $\nu_{as}^{(CH_2)}$ at 2917.8 cm^{-1}, observed for crystalline dioctadecyl dimethylammonium bromide, is used as a reference for methylene chains in an *all-trans* ordered state. The values at 2928.9 cm^{-1} and above correspond to a more disordered, liquid-like conformation of methylene chains.

In our study, the (002′) phase, signified by an interlayer spacing of 11.1 Å, is obtained either from the unfractionated redox MoS_2 dispersion or MoS_2 F1 and F2. The predominance of large-area flakes suggests that the hydrocarbon chains adopt a flat-lying orientation to the layers, thereby maximizing the vdW interactions.[4,33] This model aligns well with previously studied interlayer galleries. In conjunction with the PXRD data, IR data reveals a similar $\nu_{as}^{(CH_2)}$ at 2919.9 cm^{-1} in both NHC-functionalized unfractionated redox MoS_2 and crystalline NHC15OH[OMs] powder, indicating well-ordered methylene chains predominantly crystallized in trans conformations. Sonication-induced disturbance significantly disrupts this interlayer arrangement, as evidenced by a novel $\nu_{as}^{(CH_2)'}$ at 2956.2 cm^{-1} in redox MoS_2 1S. Upon a more precise size selection, this stretch shifts to 2917.7 cm^{-1} in the case of 15-NHC/MoS_2 F1, indicative of all-trans chains (Figure S12a). As the flake size decreases, kinks within the chains are introduced to maximize the density of organic species, characterized by a higher stretch at 2919.2 cm^{-1}, as observed in 15-NHC/MoS_2 F2 (Figure S12b). At an interlayer spacing of 13.0 Å, corresponding to the (002*) phase, a reduction in flake size introduces more kinks and increased interchain contacts, leading to a highly disordered arrangement; $\nu_{as}^{(CH_2)}$ is at 2921.9 cm^{-1} (15-NHC/MoS_2 F3) (Figure S12c). When the size reduction reaches a critical threshold (redox MoS_2 F4) (Figure S12d), efficient packing and increased interchain contacts give to stronger vdW interactions between the chains and a greater interlayer solid like character, signified by $\nu_{as}^{(CH_2)}$ shifting to 2917.7 cm^{-1}. Herein, it should be clarified that the NHC-functionalized non-fractionated redox MoS_2 and 15-NHC/MoS_2 F1 possess alkyl chains crystallized in flat-lying and trans conformations rather than upright standing and trans conformations (Figure S12a). Meanwhile, 15-NHC/MoS_2 F2 and 15-NHC/MoS_2 F3 adopt flat-lying alkyl chains crystallized in mixed conformational states, comprised of both gauche and trans conformations (Figures S12b and S12c). Similar flat-lying geometry and mixed conformational states are also observed in 15-NHC/MoS_2 1S, where structural perturbation was induced via simple sonication. In the case of 15-NHC/MoS_2 F4, the alkyl chains adopt trans conformations with a flat-lying geometry that is slightly tilted out of the plane (Figure S12d). ATIR spectra illustrating the trend in $\nu_{as}^{(CH2)}$ among the hybrid samples are shown in Figure S12e. The correlation between $\nu_{as}^{(CH2)}$ and gallery heights of NHC/MoS_2 hybrids is depicted in Figure S12f and summarized in Table S1. The combination of PXRD and ATIR data suggests that even though gallery height remains in some cases, molecular arrangement varies as a function of flake size. This variation is illustrated by a progression through different structural phases, including a phase transition from an ordered (002′) phase (15-NHC/MoS_2 F1) to a disordered (002′) phase (15-NHC/MoS_2 F2), followed by a disordered (002*) phase (15-NHC/MoS_2 F3), and ultimately to an ordered (002*) phase (15-NHC/MoS_2 F4).

Effects of Polyoxometalates (POMs). To examine the effects of adsorbed redox species on the functionalization and interlayer molecular environment of hybrid materials, analyses were conducted on two distinct dispersions: redox and CVT MoS_2. Notably, minority fractions of intercalated hybrid materials were detected across all four CVT MoS_2 dispersions, labeled as CVT MoS_2 F1−4. Additionally, only the (002′) phase, with an expanded gallery of 11.1 Å, was identified in CVT MoS_2 F1−4 samples. These phenomena can be potentially explained by two factors:

1. The size disparity: difference in platelet size between CVT MoS_2 and redox MoS_2 dispersions contribute to accelerated agglomeration. With larger platelets, such as reported CVT MoS_2, restacking happens more rapidly, due to more effective vdW forces per layer.[25]
2. Stabilizing role of POMs: POMs function as stabilizing agents, and the desorption of POMs could influence both the rate of agglomeration and the overall kinetics of functionalization.[31]

TEM images of CVT and redox MoS_2 F1 and F4 are shown in Figure S13a−d. Fractional dispersions of both CVT and redox MoS_2 show negligible differences in flake sizes. To examine the stabilizing role of POMs, NHC-functionalized CVT MoS_2 F4 was redispersed via sonication and subjected to a second cycle of NHC functionalization in DCM (NHC/MoS_2 = 15:1). The resulting hybrid, denoted as 15-NHC/MoS_2 CVT F4_2, exhibited nearly complete functionalization, characterized by an interlayer spacing of 11.1 Å, despite the small flake size (Figure S13e). ATIR analysis revealed a highly disordered structure of the organic species within the interlayer gallery, illustrated by the emergence of a unique $\nu_{as}^{(CH_2)'}$ at 2940.1 cm^{-1} (Figure S12 and Table S1). These observations suggest that POMs function as kinetic control agents, decelerating the functionalization process and thereby promoting more highly ordered SAMs on LTMD surfaces.

Robustness of Bonding. Finally, the robustness of bonding between NHCs and LTMDs was evaluated by subjecting the NHC/MoS_2 hybrid to sonication in fresh, NHC-free solvents. If NHC-LTMD bonding is weak, the NHCs will readily detach under the influence of sonication. DCM and a-ACN were selected as the fresh aprotic solvents for this evaluation. Note that, while NHC15OH[OMs] readily dissolves in DCM, the organic powder appears insoluble in a-ACN. In both solvents, the intercalated phases remain prominent, supporting that the bonding between NHCs and LTMDs is robust, and indicative of stronger interactions rather than being primarily driven by physisorption (Figure S14). In contrast, no intercalated products were observed in protic solvents such as methanol (MeOH) or ethanol. This finding is unexpected, since MeOH has been commonly reported as a suitable medium for generating free neutral NHCs. These results tentatively suggest that NHC-LTMD bonding exhibits a stronger ionic character rather than covalent bonding, which will be discussed later.

In summary, the primary points can be listed as follows:

https://doi.org/10.1021/acsanm.5c04402
ACS Appl. Nano Mater. 2025, 8, 22400−22417

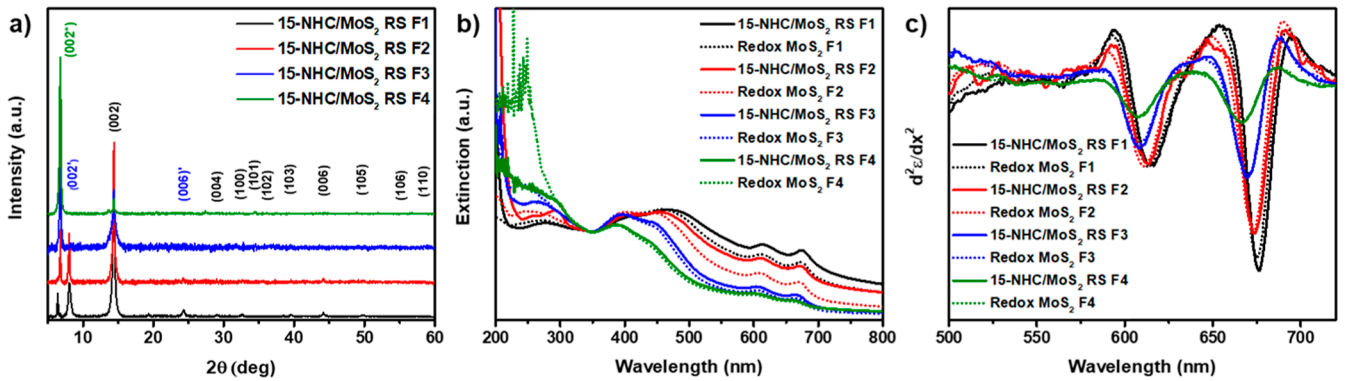

Figure 5. (a) PXRD patterns of 15-NHC/MoS_2 RS F1−4. (b) Normalized extinction spectra of 15-NHC/MoS_2 RS F1−4 in a-ACN and (c) the corresponding second derivatives of extinction spectra in (b).

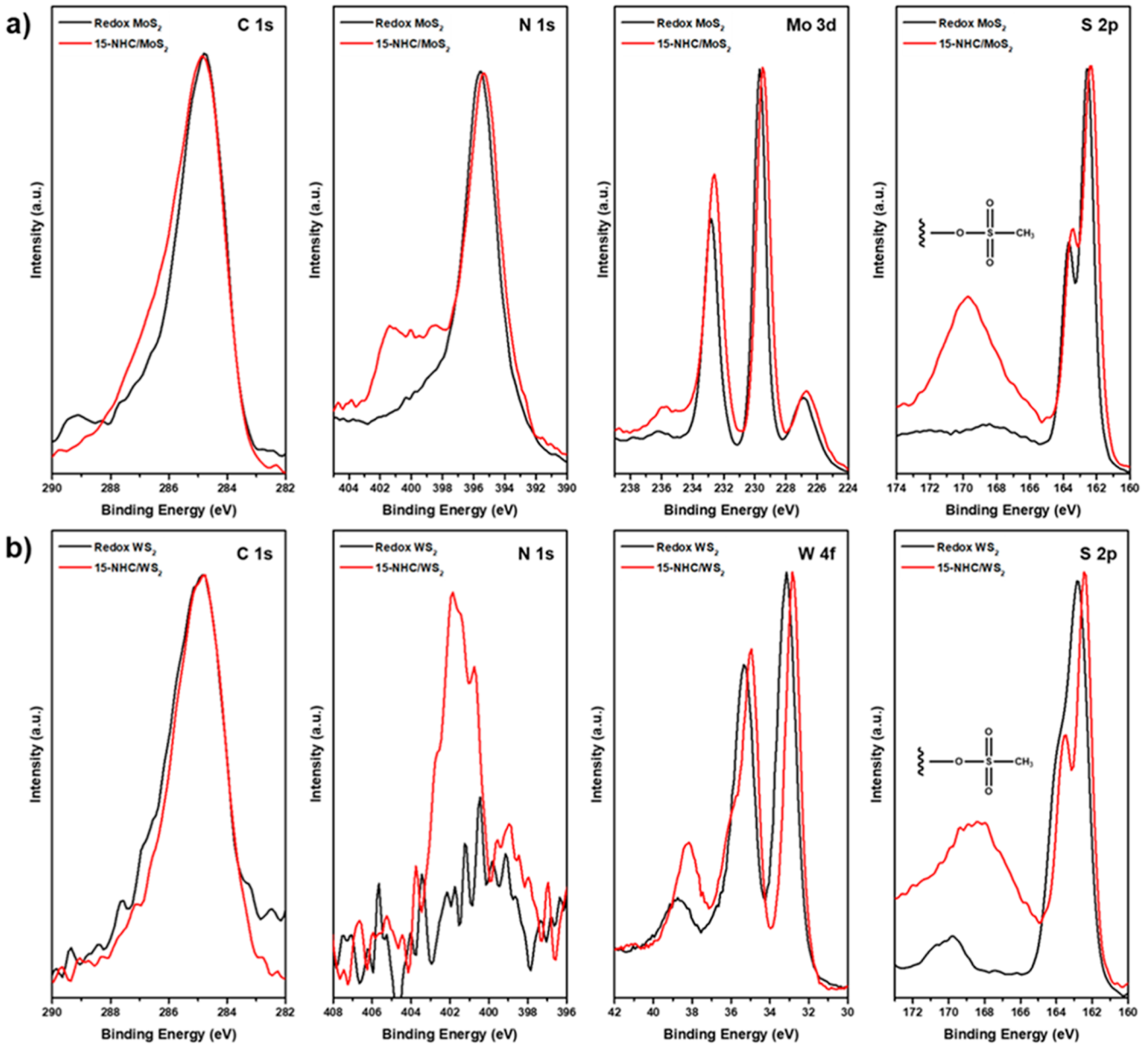

Figure 6. (a) XPS spectra of redox MoS_2 and 15-NHC/MoS_2 and (b) redox WS_2 and 15-NHC/WS_2.

https://doi.org/10.1021/acsanm.5c04402
ACS Appl. Nano Mater. 2025, 8, 22400−22417

1. The hybrid NHC-LTMD superlattice structures can be prepared using various dispersions derived using various exfoliation techniques.
2. The interactions between NHCs and Group VI LTMDs extend beyond weak physisorption. While NHCs exhibit sufficient strength to overcome the LTMD interlayer vdW attraction, the colloidal stability is altered as POMs are displaced, leading to restacking. As the POMs desorb, the colloidal stability is altered, leading to restacking. Although replacement of POMs with NHCs on the LTMD surface does not fully compensate for the loss of POMs or restore colloidal stability, it effectively creates a new potential well, leading to the formation of intercalated superstructures.
3. The formation of intercalated hybrids primarily depends on the concentration of monolayers within the dispersion. The treatment of LTMDs with NHCs, however, must occur in anhydrous aprotic solvents.
4. The molecular structures of NHC15OH[OMs]-SAMs within interlayer galleries are determined by the flake sizes, which can be modified by external perturbations.
5. Redox-active POMs are integral to the formation of intercalated hybrid superstructures as well as the interlayer structure involving organic species. Their stabilizing function is essential for establishing well-ordered SAMs within the interlayer galleries.

Characteristics of Intercalated Hybrid Superstructures. *Retained Semiconducting Properties.* The optical properties of MoS_2 change negligibly upon NHC functionalization. Figure 5 compares the extinction spectra of unfunctionalized MoS_2 dispersions to NHC/MoS_2 hybrids in a-ACN. The hybrid materials were redispersed via brief sonication, denoted as 15-NHC/MoS_2 RS F1−4. The spectral features of functionalized MoS_2 dispersions reflect their semiconducting nature, signified by the spin−orbit coupling-induced A and B excitonic transitions. These observations align with the initial hypothesis, which posits that the minimal influx of electrons into the empty conduction bands of Group VI LTMDs does not disrupt their crystallographic integrity or trigger a phase transition from semiconducting to metallic. By contrast, in the metallic state, featureless spectra are present, owing to the absence of a bandgap, as has been reported elsewhere.[34]

With hybridization, the electron density in the LTMD frameworks is expected to increase. Figure 6 compares the chemical environment and electronic configuration of unfunctionalized LTMDs and their corresponding NHC-functionalized hybrids. All spectra were initially calibrated using the C 1s peak at 284.8 eV. The spectra indicate that both exfoliated LTMDs and their corresponding functionalized hybrids retain their semiconducting features, as an intensive shift toward lower binding energy (characteristic of metallic counterparts) was not observed. Generally, this energy shift or separation has been reported to be approximately 0.8 eV, corresponding to either Mo $3d_{5/2}$ and Mo $3d_{3/2}$ peaks (as well as S $2p_{3/2}$ and S $2p_{1/2}$ peaks).[35] In the present study, a markedly smaller shift of 0.3 eV (in Mo 3d, W 4f, and S 2p), without any significant spectral shape alteration, was observed. This observation, in corroboration with the ultraviolet−visible (UV−vis) spectroscopy data further confirms the semiconducting properties of the hybrids while indicating a small *n*-doping effect. Additionally, the X-ray photoelectron spectroscopy (XPS) spectra also validate the presence of NHCs within the interlayer galleries, as illustrated by the emergence of the N 1s peak at 402 eV and the additional S 2p peak at 170 eV, associated with *N*-heterocyclic ring and methanesulfonate ($[OMs]^-$) group, respectively.

Insights into the chemical environment and the influence of NHCs on the properties of the NHC/MoS_2 and NHC/WS_2 are elucidated through deconvolution of XPS data. The deconvoluted spectra for redox MoS_2 and 15-NHC/MoS_2 are provided in Figures S15 and S16, respectively. In addition, we performed a comparative deconvolution of XPS spectra for 15-NHC/MoS_2 F4 (Figure S17), prepared from MoS_2 F4 dispersion, and its MeOH-washed counterpart, denoted as 15-NHC/MoS_2 F4W (Figure S18). As mentioned above, any treatment with protic solvent, such as MeOH, led to the collapse of intercalated structures. From the deconvolution, for C 1s, peaks at 284.8, 286.3, and 288.8 eV were attributed to C−C, C−O/C−N, and C═O, respectively. For Mo 3d, peaks at 228.5, 231.9, and 233.1 eV were attributed to Mo^{4+} $3d_{5/2}$, Mo^{5+} $3d_{5/2}$, and Mo^{6+} $3d_{5/2}$, respectively; meanwhile, peak at 226.5 eV was assigned to S 2s. The detection of $Mo^{+5/6}$ species potentially arise from oxo (Mo−O) components, which are either POMs or oxidized Mo species at flake edges, as previously documented.[15,26] For S 2p, peaks at 162.4 and 169.8 eV were assigned to S^{2-} and S^{6+} species, respectively; while the S^{6+} signal might originate both from the $[OMs^-]$ group or the oxidized S components of POMs. Deconvolution of N 1s spectra presents notable challenges due to spectral overlap between N 1s and Mo $3p_{3/2}$ peaks, which coexist closely within the same binding energy region. Accordingly, the relative ratio $Mo^{4+}/Mo^{+5/6}$ obtained from Mo 3d region was used as an internal reference to guide the fitting of the corresponding ratio $Mo^{4+}/Mo^{+5/6}$ in Mo 3p region, thereby enabling a systematic comparison. For N 1s, peaks at 395.3 and 398.1 eV were attributed to Mo^{4+} $3p_{3/2}$ and $Mo^{+5/6}$ $3p_{3/2}$, respectively, while the peak at 400.3 eV came from the *N*-heterocyclic ring. Noticeably, in 15-NHC/MoS_2 F4, two different N components, designated as N and N′, existed at 401.4 and 400.3 eV, which might arise from two different *N*-heterocyclic ring-based species. In the case of 15-NHC/MoS_2 F4W, N 1s signal was entirely absent following MeOH treatment, indicating the complete removal of NHC-based components. This corroborates with the collapse of intercalated structures, as observed in PXRD. Quantitative ratios between elements and elemental components are provided in Table S2.

From the deconvolution and derived elemental ratios, several points might be made. First, the spectral profiles of Mo 3d and S 2p regions in functionalized MoS_2 remained unchanged relative to the unfunctionalized counterpart, with no additional components derived. This suggests that interactions between NHCs or their precursors and MoS_2 do not involve the formation of covalent bonding. This interpretation aligns with up-to-date reports on surface functionalization of Group VI LTMDs, which demonstrated covalent bonding.[6,8,17,23,36] Second, a decrease in the S^{2-}/Mo ratios was observed upon exposure of redox MoS_2 to NHC15OH[OMs]. This change was accompanied by an increase in the relative abundance of S^{6+} species and $Mo^{+5/6}$ components. These variations suggest that altered chemical environment is more likely attributable to interactions with NHC15OH[OMs], rather than the retention of residual POMs. Third, the N/S^{6+} ratio is lower than 2, deviating substantially from the stoichiometry of NHC15OH-[OMs]. This discrepancy indicate additional contribution from $[OMs^-]$ anions rather than solely from the neutral carbene or its molecular cations. On the other hand, the S^{2-}/Mo ratio of redox MoS_2 was observed to differ from value of 2, indicating sulfur

https://doi.org/10.1021/acsanm.5c04402
ACS Appl. Nano Mater. 2025, 8, 22400−22417

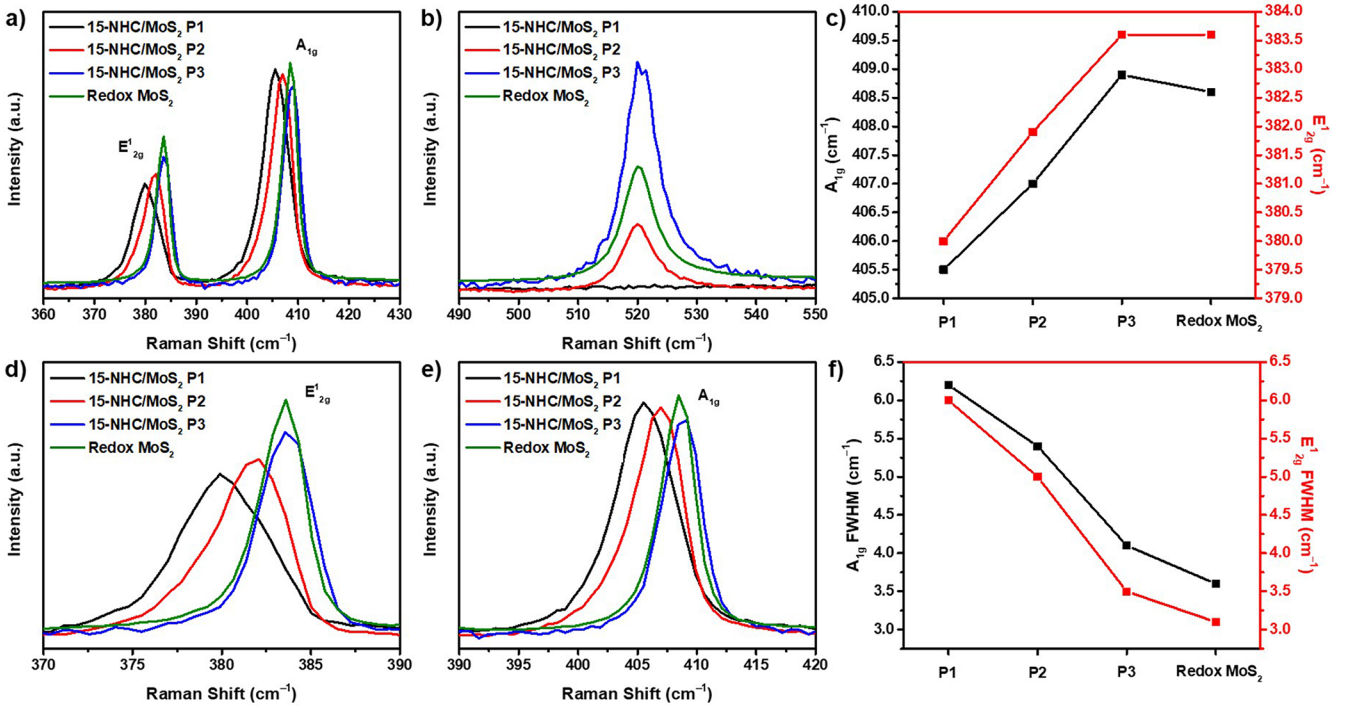

Figure 7. (a,d,e) Raman $^1E_{2g}$ and A_{1g} modes of redox MoS_2 and 15-NHC/MoS_2; the label 15-NHC/MoS_2 Px denotes data collected at different points within the same sample. (b) Si transverse optical mode as an internal reference, (c) the corresponding $^1E_{2g}$ and A_{1g} peak positions, and (f) fwhm's of $^1E_{2g}$ and A_{1g} peaks.

loss likely due to edge-site corrosion, giving to the formation of unsaturated Mo atoms at the flake edges or basal plane defects. In light of these points, it is reasonable to infer that [OMs^-] anions potentially passivate sulfur vacancies by coordinating with unsaturated Mo atoms. This passivation likely leads to Mo−O bonds, leaving to elevated oxidation states ($Mo^{+5/6}$) relatively to the Mo^{4+} in pristine MoS_2. However, the coordination of [OMs^-] anions to unsaturated Mo atoms did not lead to the final intercalated structures, as performed in the case of 15-NHC/MoS_2 F4W, in which N 1s signal was completely absent; despite that S^{6+} signal remained dominant. These results collectively support the hypothesis that the intercalated structures arise from interactions on the basal plane between MoS_2 and the molecular cations bearing *N*-heterocyclic rings. A similar observation was recorded for NHC/WS_2 hybrids. To enrich the content of monolayer flakes, an exfoliated WS_2 dispersion collected at a centrifuge rate of 4000 rpm was subjected to NHC functionalization. The resulting hybrid is designated as 15-NHC/WS_2 4k. Deconvolution data and quantitative ratios between elements and elemental components are provided in Figures S19−S21 and Table S3.

Vibrational Characteristics. Phonon Raman scattering, which arises from the lattice vibrations of materials, is regarded as a diagnostic tool for characterizing the lattice structures, determining layer numbers, and accessing doping and strain conditions within 2D LTMDs. Certain features of the Raman spectra can provide insight into phonons, electron−phonon, and electron−electron interactions of the NHC-LTMD hybrid materials. In the case of "untreated" semiconducting MoS_2, the Raman spectra yield two intrinsic Raman modes: in-plane $^1E_{2g}$ and out-of-plane A_{1g}. In particular, the interval between these two peaks is a reliable indicator of the number of layers of MoS_2 flakes. Usually, a peak separation of approximately 19 cm^{-1} is characteristic of monolayer MoS_2, while the intervals of 20−23 correspond to bi- and trilayer MoS_2, and a separation of 25 cm^{-1} is indicative of multilayer MoS_2.[37] However, these trends are most commonly observed in well-defined, large-area MoS_2 monolayers (up to μm scale) synthesized via chemical vapor deposition (CVD). In such systems, the MoS_2 monolayers are generally regarded as undoped, exhibit minimal defect concentrations, and are not affected by additional factors such as dielectric screening effects.[29] In contrast, solution-processed systems often exhibit altered vibrational characteristics due to the influence of multiple factors involving in the specific exfoliation and processing methods employed, which can introduce partial doping and structural disorder into the material. This phenomenon, commonly referred to as procedure-dependent properties, has been documented through a systematic study involving several exfoliated MoS_2 dispersions prepared using different solution-processing methods.[26] Notably, in such systems, both $^1E_{2g}$ and A_{1g} Raman modes of exfoliated MoS_2 displayed a concomitant shift in the same direction. Other studies reported that the directional shift of either $^1E_{2g}$ or A_{1g} exhibited distinct behaviors under specific conditions. The $^1E_{2g}$ mode is more sensitive to in-plane strain, whereas the A_{1g} mode is more responsive to doping.[38,39] These trends lead to the fact that the solution-processing techniques impart both surface strain and doping effects to the exfoliated MoS_2 flakes. Consequently, the peak separation for the monolayer architecture of solution-processed MoS_2 varies more than 19 cm^{-1} in certain systems (Figure S22). Given the heterogeneous nature of exfoliated dispersions, it is crucial to acknowledge that the Raman modes reflect a population median comprising both mono- and few-layered flakes. In addition, isolating and analyzing only monolayer flakes—particularly below 100 nm in lateral dimensions—poses challenges during sample. Therefore, Raman data from solution-processed systems should be interpreted with caution and contextualized differ-

https://doi.org/10.1021/acsanm.5c04402
ACS Appl. Nano Mater. 2025, 8, 22400−22417

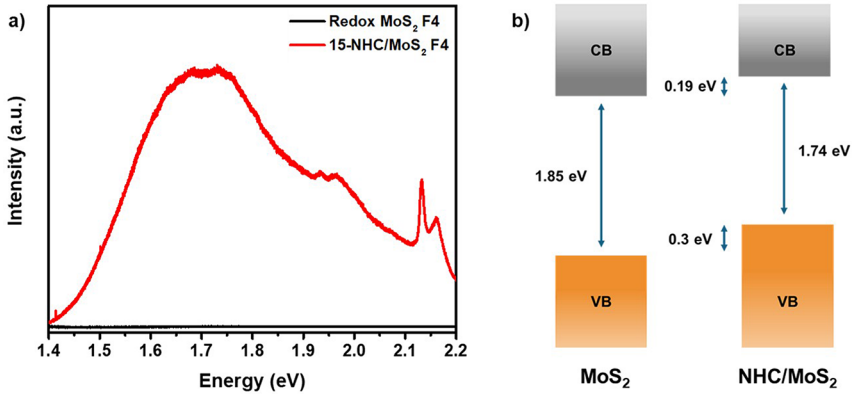

Figure 8. (a) Photoluminescence of redox MoS_2 F4 and 15-NHC/MoS_2 F4. (b) Constructed bandgap diagrams of MoS_2 and NHC-functionalized MoS_2.

ently from those obtained from conventional CVD methods. Finally, depending on the behaviors of the in-plane and out-of-plane modes, information regarding lattice structures, surface strain, and doping types can be extracted.

Figure 7 compares the $^1E_{2g}$ and A_{1g} modes of redox MoS_2 and 15-NHC/MoS_2. For systematic and comprehensive data collection, all samples were deposited onto 300 nm SiO_2/Si substrates, taking advantage of the Si optical transverse vibration mode as an internal reference. To avoid ambient moisture adsorption, which has been reported to partially dope LTMDs,[29] after complete solvent evaporation, the samples were stored in an environment enriched with $CaSO_4$ desiccant under vacuum prior to any measurements. Note that Raman spectra of three different points within a single 15-NHC/MoS_2 sample, labeled as 15-NHC/MoS_2 P1−3, were acquired within the same day. Although the Si optical transverse mode completely diminished in 15-NHC/MoS_2 P3 due to the thick layer of deposited materials, peak shift issues were avoided due to repetitive calibration. The data show that vibrational behavior varies between three points taken, which can be attributed to the heterogeneity of the exfoliated dispersion, as discussed previously. Within the restacked hybrid superstructures, it is evident that the NHCs have a pronounced effect on enriched-monolayer regions (P1, P2) but have a comparatively modest influence on the few-layered region (P3), which behave similar to redox MoS_2. In general, 15-NHC/MoS_2 P1 and P2 can be regarded as being primarily composed of the (002′) or (002*) phase, whereas 15-NHC/MoS_2 P3 consists exclusively of the (002) phase (Scheme 2). Notably, both $^1E_{2g}$ and A_{1g} modes for 15-NHC/MoS_2 P1 and P2 exhibited a major red shift (∼3.5 cm^{-1}), suggesting the presence of both in-plane layer strain and an *n*-doping effect.[38,40−43] In addition to peak shift, the broadening and the evolving asymmetry of both $^1E_{2g}$ and A_{1g} peaks were detected. As the $^1E_{2g}$ and A_{1g} two modes undergo further red shifting, their full widths at half-maximum (fwhm's) increase accordingly. These changes have been interpreted as partially independent parameters that can be used to assess surface strain and doping levels, assuming that both effects are decoupled from each other.[44] The peak changes observed for the 15-NHC/MoS_2 hybrid are consistent with a model in which the NHCs not only transfer their electrons, which dissipate and delocalize across the monolayers, but also induce modifications to the lattice structure of MoS_2 and apply major strain (generating lattice disorder) to the in-plane monolayers. Similar trends were observed for the 15-NHC/WS_2 hybrid (Figure S23).

Given the persistent challenge of heterogeneity, the observed vibrational characteristics of the hybrid materials are likely due to collective effects. To explore this hypothesis, functionalized hybrids of individual fractional dispersions were prepared and subsequently analyzed (Supplementary Note 2, Figure S24, Tables S4 and S5). The extracted $A_{1g}/^1E_{2g}$ ratios illustrate substantial deviations in the lattice structures of the hybrid materials compared to unfunctionalized MoS_2. This disordered lattice fashion, induced by the interactions between NHCs and out-of-plane Mo−S vibrations, is supported by the splitting in the (002) reflection, a characteristic feature of restrained MoS_2 layers (Figure S14).[45] From the peak positions of $^1E_{2g}$ and A_{1g} modes, carrier doping concentration and NHC-induced strain were determined to be $197.58 \pm 0.19 \times 10^{13}$ cm^{-2} per layer and 0.58% increase in strain, respectively, compared to that of redox MoS_2. This doping concentration is comparable to the recently reported studies of heavily *n*-doped MoS_2 via electrochemistry-induced molecular intercalation (3.55×10^{15} cm^{-2} per layer).[40] To mitigate the impact of heterogeneity, information derived from 15-NHC/MoS_2 F4 is considered more reliable for discussion, given its nearly complete NHC functionalization. Calculation methods and extended discussions related to Raman analysis of functionalized hybrids derived from individual fractional dispersions are provided in Supplementary Note 2, Figure S24, Tables S4 and S5.

Monolayer Behavior of Hybrid Superlattice Structures. Recent theoretical[21] and experimental[21,32,46] studies have suggested that certain *n*-doped hybrid superlattice structures exhibit semiconducting monolayer behavior, as indicated by detectable photoluminescence (PL) from molecular-intercalated bulk monolayer MoS_2.[21,32,46] These intercalated systems bear certain similarities to our systems, which are characterized by two key features:

1. The intercalated species within the interlayer galleries effectively overcome the interlayer attraction and coupling in LTMDs. Consequently, even as restacked superlattice structures, our hybrid materials retain the physical and optical properties of their monolayer components.
2. The amount of doped electrons is insufficient to trigger a phase transformation (1H semiconducting to 1T metallic).

Figure 8a illustrates the PL signal observed in 15-NHC/MoS_2 F4, which was also detected in the three other fractional hybrids (Figure S25). Note that these PL signals originate from solid

https://doi.org/10.1021/acsanm.5c04402
ACS Appl. Nano Mater. 2025, 8, 22400−22417

samples—the intercalated hybrid powders. These powders were used to prepare thin films, which were subsequently subjected to measurement. In contrast, no PL signal was detected in any of four fractional redox MoS_2 samples, owing to self-restacking and the re-establishment of interlayer coupling. Given the potential PL activity of the aromatic *N*-heterocyclic ring, a control experiment was conducted to verify the origin of the observed PL signal. The results confirmed that the PL emission originated from the intercalated hybrids (Figure S26). Despite the outstanding phenomenon arising from a multimonolayer structure, the PL peaks of NHC/MoS_2 hybrids appear in the range of 1.65−1.75 eV, which is lower than the optical bandgap of undoped monolayer MoS_2 (1.85 eV).[47] We assign these PL peaks to the A-excitonic direct transition at the *K*-point, ruling out the possibility that it primarily originates from negatively charged excitons, or A^- trions. This assignment is supported by two critical points: (1) the introduction of NHCs induce tensile strain, which modifies the lattice structure and leads to an alteration of bandgaps. Consequently, both A excitons and A^- trions undergo a red shift;[42] and (2) in an exclusively *n*-doped system, the peak position and PL intensity of A^- trions remains constant, while the PL intensity of A excitons is significantly suppressed.[48,49] In our findings, the PL peaks of hybrid superstructures, instead, exhibit a blue shift across four fractional dispersions, with the highest PL energy recorded at 1.74 eV for 15-NHC/MoS_2 F4. We attribute this bandgap modification to the combined effects of applied tensile strain and *n*-doping levels introduced by NHC functionalization.[40] We argue that the tensile strain and *n*-doping levels can be tentatively assessed by the molecular packing density, which is governed by the flake sizes. Assuming that larger flakes accommodate a higher content of intercalated organic species, the optical bandgaps of corresponding superlattice structures are further red-shifted, as shown in Figure S25.

The impact of defects on the PL performance should not be overlooked, particularly in the context of solution-processed approaches, which often yield flakes with high density of defects. In the case of redox MoS_2 and redox WS_2, sulfur vacancies and unsaturated Mo and W atoms arise as an inherent byproduct of the redox driven exfoliation mechanism. In general, these defects might act as trapping sites for electron−hole recombination, thereby suppressing overall PL signals,[50] or alternatively, introducing additional energy states giving to defect-related PL emissions.[51] In our study, across all functionalized hybrids F1−4, the incomplete intercalation, owing to heterogeneity, did not yield fully separated monolayer components; therefore, comparisons based on PL intensity are considered unreliable. The PL spectra of all hybrid samples exhibited broad emission profiles yet did not display features associated with defect-related states in the lower energy regions. Note that, the defect sites are primarily localized at flake edges, and these defects are potentially passivated by [OMs^-] anions or neutral NHCs as previously discussed. Therefore, despite the impact being significant, based on the experimental observations, it remains challenging to draw definitive conclusions regarding the defect density of these redox material-based hybrids. From other perspectives, the broadening and red-shift of the PL emissions, as shown in this study, resemble the behavior reported for molecular cation-intercalated single crystal 2H Group VI LTMDs, in which the intercalated MoS_2 showcased broad PL profiles, with emission energies shifting as a function of the electron doping level.[40] In the reported work, the Raman behavior, corroborating with XPS data, aligns closely with our experimental findings and collectively reinforces the interpretation that the doping content and lattice strain are introduced through surface functionalization.

Finally, we constructed the bandgap diagram of hybrid NHC/MoS_2, which is shown in Figure 8b. The diagram was constructed using PL information extracted from 15-NHC/MoS_2 F4, selected to minimize the effects of heterogeneity. The energy variation in the valence band was estimated, using the low-energy region of the XPS spectra, providing a measure of the energy gap between the valence band and the Fermi level (Figures S27 and S28). The optical bandgap of undoped monolayer MoS_2 was used as a comparative reference, enabling the inference of the relative conduction band position of the hybrid.

Nature of NHC-LTMD Interactions—Ionic Bonding Model. In pursuit of a comprehensive understanding of the fundamental interactions between NHCs and Group VI LTMDs, we reviewed the literature reporting the formation of covalent bonds. These studies underscore notable alterations in the XPS profiles of the d orbitals of transition metals and the p orbitals of chalcogens within the analyzed LTMDs.[6,17,19,52] Before delving into a detailed discussion of the interactions, electronic configurations, and other related phenomena, we highlight several key preliminary considerations:

1. Injection or removal of charge in the layer would change the orbital occupancy and drive a lattice change, which would shift the materials properties from semiconducting (2H) to metallic (1T). This transition would be accompanied by changes in the in-plane lattice structure and the registry of the lattices between interlayers.[5,22,53]
2. If a strong Lewis acid/base reaction were to occur, substantial charge injections would be introduced. Consequently, an appropriate number of balancing cations would be needed to maintain charge neutrality and stability of the newly formed structures, as exemplified in the case of Li intercalation.[54]
3. Charge injections into the antibonding orbitals, or partially occupied orbitals, would significantly increase the materials' reactivity and modify the optoelectronic properties. For instance, if charge injection changed the LTMD to 1T, it could be changed back to 2H if electrons were transferred from the LTMD to some other species; however, if covalent bond formation were to occur, the 1T phase would be stabilized and persist.[6,36,55] Alongside strong covalent bonding, ionic interactions that balance the excess charge would also maintain the structural integrity of the 1T phase.[32]
4. If a physisorption process were to take place, involving either vdW or dipolar interactions, charge injection would be unexpected, as it would lead to relatively weak interactions with the surface, as described in surface/matching mechanism for stabilized dispersions.[10,13]

In our study, a small shift to the lower binding energy (charge injection), without any significant changes in the XPS spectral profiles, likely indicates interactions that fall between strong covalent bonding and physisorption. This proposal is further supported by the results of sonication experiments conducted in anhydrous aprotic and protic solvents. Note that the carbene used in this study remains in its precursor form as a salt rather than existing as the commonly accepted neutral carbene. This benzimidazolium salt is often referred to as a "masked carbene" due to its behavior resembling that of a neutral carbene.[56−59] In

https://doi.org/10.1021/acsanm.5c04402
ACS Appl. Nano Mater. 2025, 8, 22400−22417

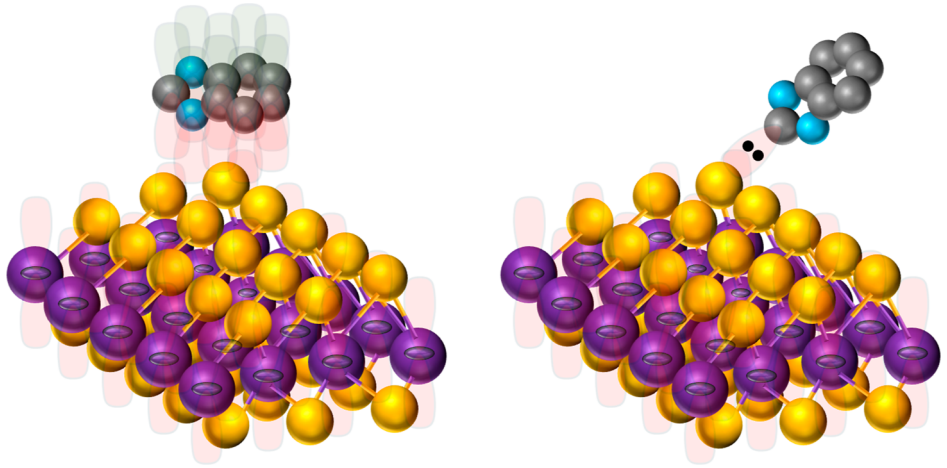

Figure 9. Parallel alignment of the *N*-heterocyclic ring to the LTMD layers (left) and the potential scenario of orbital hybridization from the in-plane lone pair electrons to the chalcogen p_z orbitals (right).

protic solvents, the precursor undergoes hydrolysis, yielding the neutral carbene, a phenomenon that is well documented and used for the formation of SAMs on gold surfaces.[24,60−62] In contrast, based on our experience, SAMs formed on gold surfaces in aprotic solvents, such as DCM, exhibit poorly ordered films, likely due to insufficient formation of free "unmasked" carbene in the aprotic solvent. Recently, computational and experimental findings have revealed some inconsistencies, while proposing hypotheses that align with our work. From a theoretical standpoint, it was reported that neutral NHC was unlikely to form covalent bonds with 2H Group VI LTMDs.[63,64] In contrast, contemporaneous with the submission of our manuscript, Hersam's group showed experimental evidence indicating potential covalent interactions between neutral NHCs and the basal plane of semiconducting WS_2 monolayers.[23] However, it should be noted that neutral NHCs might primarily function to passivate chalcogen defect sites—such as unsaturated W atoms—rather than forming covalent bonds with the chalcogenide atoms, as suggested by other study.[65] Based on both literature reports and our own observations concerning the degradation of hybrid superlattice structures in protic solvents, two keys question arise: (1) do the interactions with LTMDs involve the neutral NHCs or their benzimidazolium salts? (2) What is the fundamental nature of these interactions?

In our work, XPS data indicate that the interlayer galleries of the hybrid superstructures are composed of the salt precursor, as confirmed by the presence of S^{6+} originating from the $[OMs]^-$ groups. Further, charge injection into LTMDs renders a negative charge on the layers, which shifts the spectral profiles toward lower binding energies across all Mo, W, and S core-level regions. This observed trend contrasts with the trend expected for covalent bonding, as claimed by Hersam and colleagues.[23] Two distinct N components were also recorded in our XPS data for both 15-NHC/MoS_2 F4 and 15-NHC/WS_2 4k (Figures S17 and S21), in agreement with the N 1s features reported by Hersam and co-workers. However, following MeOH washing, the N 1s signal was entirely absent, casting doubt on the formation of covalent bonds in our case. On the other hand, our system share certain similarities to the molecular cations-intercalated single crystal Group VI LTMDs via an electrochemically anode-driven approach, wherein molecular cations are driven to compensate for the excess electron injection into the materials induced through an applied negative voltage.[21,40] Consequently, the interaction is better represented by a simple ionic model, wherein a charge-balancing process between the negatively charged LTMD layers and the *N*-heterocyclic ring-based cations of the benzimidazolium salts predominates. This phenomenon has been previously described as "homosolvation and Lewis base intercalation", as reported in the cases of pyridine or NH_3.[66] We hypothesize that a minority fraction of neutral NHCs generated in aprotic solvents partially reduces the LTMDs to give negatively charged layers.[67,68] Subsequently, the protonated cations of NHC15OH[OMs] are electrostatically attracted to balance the excess negative charge on the LTMDs. This ionic bonding is consistent with the observed parallel alignment of the *N*-heterocyclic ring, which maximizes the Coulombic interaction. In contrast, complete hydrolysis in protic solvents eliminates the molecular cations, leaving none available for subsequent interactions. As a consequence of the parallel alignment, the π-electron system, arising from p_z to p_z hybridization between the conjugated rings and the chalcogen layers, is maximized.[69] The strength of this interaction surpasses the vdW forces between LTMD layers, facilitating the monolayer-like behavior of the hybrid superstructures. Notably, despite the electron injection from the partial reduction induced by the neutral NHCs, the lone pair electrons residing in the in-plane *N*-heterocyclic ring have the potential to hybridize with the p_z orbitals of the chalcogen layers,[63,64] as illustrated in Figure 9. Nevertheless, considering the differing use of neutral versus masked NHCs in our study compared to recent reports, it is plausible that the nature of interaction—whether ionic or covalent—varies depending on the specific chemical conditions.

CONCLUSIONS

In summary, we have demonstrated the first experimental approach to fabricating superlattice structures via the functionalization of Group VI LTMDs with masked NHCs. We demonstrated that this chemistry is effective across multiple types of exfoliated LTMD dispersions, including those consisting of MoS_2 and WS_2. The results indicate that Lewis acid−base chemistry can be used not only for metallic LTMDs, but also for semiconducting LTMDs by extracting a gentle influx of electrons from the organic ligands, partially populating the orbitals that compose the conduction bands of the LTMDs. The functionalization occurs exclusively on the surface (basal plane)

https://doi.org/10.1021/acsanm.5c04402
ACS Appl. Nano Mater. 2025, 8, 22400−22417

of the exfoliated 2D flakes, initiated by the partial reduction of the layers and subsequently stabilized by ionic interactions with the NHC precursors. The resulting restacked superlattice structures, with interlayer structures governed by the heterogeneity of exfoliated dispersions, retain semiconducting properties. Experimental observations indicate that the interaction strength between the LTMD and the organic intercalators exceeds the interlayer vdW forces between LTMD layers, rendering the observed monolayer-like characteristics. Importantly, we demonstrate for the first time that this solution-based approach does not lead to an extensive optical bandgap change. Taken together, our findings introduce a new strategic approach to functionalize semiconducting Group VI LTMDs and present a new family of intercalated materials based on the framework of the LTMD hosts and the NHC family. With the developed chemistries presented, novel opportunities to expand the applications of LTMDs across advanced technological platforms are unlocked.

EXPERIMENTAL SECTION

Materials. Molybdenum disulfide (MoS_2, <2 μm), tungsten disulfide (WS_2, <2 μm), hydroquinone (HQ), cumene hydroperoxide (CHP), anhydrous acetonitrile (a-ACN), sodium borohydride ($NaBH_4$), sodium thiocyanate (NaSCN), sodium molybdate (Na_2MoO_4), sodium tungstate dihydrate ($Na_2WO_4{\cdot}2H_2O$), pentadecalactone, hydrobromic acid (48 wt %), dicyclohexylcarbodiimide (DCC), 4-(dimethylamino)pyridine (DMAP), 4-amino-3-nitrophenol, potassium carbonate (K_2CO_3), lithium aluminum hydride ($LiAlH_4$), iron powder 325 mesh (Fe), ammonium chloride (NH_4Cl), isopropyl methanesulfonate, cesium carbonate (Cs_2CO_3), acetic acid (AcOH), methanol (MeOH), dichloromethane (DCM), acetonitrile (ACN), formic acid (HCOOH), isopropyl alcohol (IPA), and tetrahydrofuran (THF) were purchased from Sigma-Aldrich, USA. Hydrochloric acid was purchased from Oakwood Chemical, USA. Water was purified to a resistance of 18 MΩ-cm, employing an Academic Milli-Q Water System (Millipore Corporation) and filtered through a 0.22 μm membrane before use. Silica gel for column chromatography was obtained from Sorbent Technologies. CVT grown MoS_2 powder was prepared as reported elsewhere.[25]

Methods. Experimental methods, including synthesis of adsorbates, redox exfoliation of MoS_2, redox exfoliation of WS_2, bath sonication-induced exfoliation, thin-film fabrication, size selection by centrifuge cascade, functionalization of exfoliated LTMDs by NHC adsorbates, and NHC functionalization of exfoliated LTMDs under sonication, are detailed in the accompanying Supporting Information file in page S2 to page S7.

Characterizations. A Cary 60 UV−vis spectrophotometer was used for all extinction measurements; UV−vis technical parameters, data analysis and mathematical transformation (second derivative of extinction spectrum and corresponding smoothing steps) were followed as the protocol previously reported.[70] A scanning electron microscope (SEM) LEO-1525 with an accelerating voltage of 15 kV and a JEOL JEM-2010 transmission electron microscope (TEM) operating at an accelerating voltage of 200 kV were used for imaging. Atomic force microscopy (AFM) characterization was performed using AFM, MFP-3D Origin+, Oxford Instruments in a noncontact soft tapping mode; the AFM tips utilized were Bruker TESPA-V2 model. The powder X-ray diffractometer (PXRD, Smart Lab, Rigaku, Cu Kα radiation (λ = 0.15406 nm) operated at 40 kV and 44 mA, 5 mm beam mask, 1/8° divergence slit, step size 0.02° (2θ), scanning rate 1.5° min^{-1}) was used for all crystallographic analysis. The infrared (IR) measurements were performed employing an ATR-IR, Nicolet iS10, Thermo Scientific in the range of 500−4000 cm^{-1} with 2 cm^{-1} resolution. Zeta potential measurements were taken on diluted exfoliated LTMD dispersions (0.01 mM) and NHC-functionalized LTMD dispersions (0.01 mM) in ACN using a dip cell that is compatible with organic solvents; measurements were performed on a Malvern Zetasizer model ZEN3600. X-ray photoelectron spectroscopy (XPS) analysis was carried out using a PHI 5700 X-ray photoelectron spectrometer equipped with a monochromatic Al Kα source with 10 mA emission current and 15 kV emission bias; all spectra were calibrated by the C 1s peak at 284.8 eV. The Raman scattering spectra were measured using a Horiba JY T64000 triple spectrometer. The spectrometer was coupled with an Olympus optical microscope, which focused the 488 nm laser beam on the samples using 50× or 100× objectives, collected the scattered light, and directed it to the spectrometer. The laser power was maintained at minimum, typically below 10^3 W/cm^2, to prevent overheating or phase transformation of the samples. All spectra were recorded in the backscattering configuration, with incident and scattered light propagating perpendicular to the sample surfaces. The photoluminescence (PL) and Raman scattering spectra of centrifuge cascade fractions and their corresponding functionalized fractions were measured using a Renishaw inVia using a 532 nm laser with a 50× LWD objective with a numerical aperture of 0.75 and an 1800 lines/mm grating. All spectra were collected with a 60 s acquisition time at 10% laser power (606 μW). Baselines from the spectra were corrected using asymmetrically reweighted penalized least-squares smoothing before fitting with pseudo-Voigt line shapes. Additional details about characterization by AFM, Raman spectroscopy, and PL can be found in the Characterization Notes on page S7 in the Supporting Information.

ASSOCIATED CONTENT

Data Availability Statement

The data that support the findings of this study are available from the corresponding author upon reasonable request.

Supporting Information

The Supporting Information is available free of charge at https://pubs.acs.org/doi/10.1021/acsanm.5c04402.

Experimental methods: synthesis of adsorbates; redox exfoliation of MoS_2; redox exfoliation of WS_2; bath sonication-induced exfoliation; size selection by centrifuge cascade (method and Scheme S1); thin-film fabrication (method and Scheme S2); functionalization of exfoliated LTMDs by NHC adsorbates, NHC functionalization of exfoliated LTMDs under sonication; characterization notes for AFM, Raman spectroscopy, and PL; AFM characterization of MoS_2 nanoflakes (Figure S1); extinction spectra and second derivatives of redox WS_2 dispersions (Figure S2); AFM characterization and PXRD of WS_2 nanoflakes (Figures S3 and S4); surface Zeta potentials of redox MoS_2 (Figure S5); extinction spectra and the extracted titration fitting of MoS_2 (Figure S6) and WS_2 (Figure S7); Supplementary Note 1: a mini review of intercalated layered materials (Figures S8 and S9); PXRD patterns of NHC15OH[OMs] intercalated MoS_2 and WS_2 (Figure S10); Zeta potentials of redox MoS_2, bath-sonication MoS_2, and 15-NHC/MoS_2 (Figure S11); ATIR spectra of NHC15OH[OMs] intercalated MoS_2 (Figure S12); summary of ATIR and PXRD data of NHC15OH[OMs] intercalated MoS_2 (Table S1); TEM images of redox and CVT MoS_2 and PXRD patterns of NHC15OH[OMs] intercalated CVT MoS_2 (Figure S13); PXRD patterns of sonicated NHC15OH[OMs] intercalated MoS_2 (Figure S14); deconvoluted XPS spectra of redox MoS_2, 15-NHC/MoS_2, 15-NHC/MoS_2 F4, and 15-NHC/MoS_2 F4W (Figures S15−18); elemental ratios from deconvoluted XPS spectra for NHC/MoS_2 (Table S2); deconvoluted XPS spectra of redox WS_2, 15-NHC/WS_2, 15-NHC/WS_2 4k (Figures S19−S21); elemental ratios from deconvoluted XPS spectra for NHC/WS_2 (Table S3); peak

https://doi.org/10.1021/acsanm.5c04402
ACS Appl. Nano Mater. 2025, 8, 22400−22417

intervals of $^1E_{2g}$–A_{1g} of NHC15OH[OMs] intercalated MoS_2 and WS_2 (Figure S22); Raman spectra of NHC15OH[OMs] intercalated WS_2 (Figure S23); Supplementary Note 2: additional Raman analysis (Figure S24 and Tables S4 and S5); PL of NHC15OH-[OMs] intercalated MoS_2 fractions (Figure S25); PL of NHC15OH[OMs] powder (Figure S26); XPS low-energy region of NHC15OH[OMs] intercalated MoS_2 (Figure S27) and NHC15OH[OMs] intercalated WS_2 (Figure S28) (PDF)

AUTHOR INFORMATION

Corresponding Authors

Richard A. Vaia − *Materials and Manufacturing Directorate, Air Force Research Laboratory, Dayton, Ohio 45433, United States;* orcid.org/0000-0003-4589-3423; Email: richard.vaia@us.af.mil

T. Randall Lee − *Department of Chemistry and the Texas Center for Superconductivity, University of Houston, Houston, Texas 77204-5003, United States;* orcid.org/0000-0001-9584-8861; Email: trlee@uh.edu

Authors

Quoc Minh Tran − *Department of Chemistry and the Texas Center for Superconductivity, University of Houston, Houston, Texas 77204-5003, United States;* orcid.org/0009-0006-8244-3236

Yunsoo Choi − *Department of Chemistry and the Texas Center for Superconductivity, University of Houston, Houston, Texas 77204-5003, United States*

Nikolaos Chalmpes − *Department of Materials Science and Engineering, Cornell University, Ithaca, New York 14850, United States;* orcid.org/0000-0003-2744-5934

Drake Austin − *Materials and Manufacturing Directorate, Air Force Research Laboratory, Dayton, Ohio 45433, United States*

Supawitch Hoijang − *Department of Chemistry and the Texas Center for Superconductivity, University of Houston, Houston, Texas 77204-5003, United States;* orcid.org/0000-0002-0061-5166

Melissa Ariza Gonzalez − *Department of Chemistry and the Texas Center for Superconductivity, University of Houston, Houston, Texas 77204-5003, United States;* orcid.org/0009-0009-7900-5835

Minh Dang Nguyen − *Department of Chemistry and the Texas Center for Superconductivity, University of Houston, Houston, Texas 77204-5003, United States;* orcid.org/0000-0002-2569-8279

Pailinrut Chinwangso − *Department of Chemistry and the Texas Center for Superconductivity, University of Houston, Houston, Texas 77204-5003, United States;* orcid.org/0009-0001-0691-8969

Viktor G. Hadjiev − *Department of Mechanical Engineering and the Texas Center for Superconductivity, University of Houston, Houston, Texas 77204-5003, United States*

Arnold M. Guloy − *Department of Chemistry and the Texas Center for Superconductivity, University of Houston, Houston, Texas 77204-5003, United States;* orcid.org/0000-0003-2492-4323

Allan J. Jacobson − *Department of Chemistry and the Texas Center for Superconductivity, University of Houston, Houston, Texas 77204-5003, United States;* orcid.org/0000-0002-6540-8846

Nicholas R. Glavin − *Materials and Manufacturing Directorate, Air Force Research Laboratory, Dayton, Ohio 45433, United States;* orcid.org/0000-0002-9447-7509

Complete contact information is available at: https://pubs.acs.org/10.1021/acsanm.5c04402

Author Contributions

Q. M. T.: Conceptualization; Formal analysis; Investigation; Methodology; Validation; Writing—original draft. Y. C., S.H., M. A. G., V. G. H.: Methodology. N. C.: Formal analysis; Writing—review and editing. D. A.: Methodology; Writing—review and editing. N. R. G.: Methodology; Resources. M. D. N., P. C.: Visualization; Writing—review and editing. A. M. G., A. J. J.: Formal analysis. R. A. V.: Formal analysis; Investigation; Methodology; Resources; Supervision; Validation; Writing—review and editing. T. R. L.: Conceptualization; Formal analysis; Funding acquisition; Project administration; Supervision; Writing—review and editing.

Notes

The authors declare no competing financial interest.

ACKNOWLEDGMENTS

This work was generously supported by the Robert A. Welch Foundation (Grant No. E-1320 and Grant No. E-0024) and the Air Force Office of Scientific Research (FA9550-23-1-0581; 23RT0567). We thank Dr. Michael A. Susner for providing the CVT MoS_2 employed in this study.

REFERENCES

(1) Chhowalla, M.; Shin, H. S.; Eda, G.; Li, L.-J.; Loh, K. P.; Zhang, H. The Chemistry of Two-Dimensional Layered Transition Metal Dichalcogenide Nanosheets. *Nat. Chem.* **2013**, *5*, 263−275.

(2) Ippolito, S.; Kelly, A. G.; Furlan de Oliveira, R.; Stoeckel, M.-A.; Iglesias, D.; Roy, A.; Downing, C.; Bian, Z.; Lombardi, L.; Samad, Y. A.; Nicolosi, V.; Ferrari, A. C.; Coleman, J. N.; Samorì, P. Covalently Interconnected Transition Metal Dichalcogenide Networks via Defect Engineering for High-Performance Electronic Devices. *Nat. Nanotechnol.* **2021**, *16*, 592−598.

(3) Canton-Vitoria, R.; Sayed-Ahmad-Baraza, Y.; Pelaez-Fernandez, M.; Arenal, R.; Bittencourt, C.; Ewels, C. P.; Tagmatarchis, N. Functionalization of MoS_2 with 1,2-Dithiolanes: Toward Donor-Acceptor Nanohybrids for Energy Conversion. *npj 2D Mater. Appl.* **2017**, *1*, 13.

(4) Wang, J.; Yu, H.; Zhou, X.; Liu, X.; Zhang, R.; Lu, Z.; Zheng, J.; Gu, L.; Liu, K.; Wang, D.; Jiao, L. Probing the Crystallographic Orientation of Two-Dimensional Atomic Crystals with Supramolecular Self-Assembly. *Nat. Commun.* **2017**, *8*, 377.

(5) Eda, G.; Fujita, T.; Yamaguchi, H.; Voiry, D.; Chen, M.; Chhowalla, M. Coherent Atomic and Electronic Heterostructures of Single-Layer MoS_2. *ACS Nano* **2012**, *6*, 7311−7317.

(6) Voiry, D.; Goswami, A.; Kappera, R.; Silva, C.; Kaplan, D.; Fujita, T.; Chen, M.; Asefa, T.; Chhowalla, M.; Chhowalla, M. Covalent Functionalization of Monolayered Transition Metal Dichalcogenides by Phase Engineering. *Nat. Chem.* **2015**, *7*, 45−49.

(7) Tuci, G.; Rossin, A.; Pham-Huu, C.; Mosconi, D.; Luconi, L.; Agnoli, S.; Granozzi, G.; Giambastiani, G. Multimodal Hybrid 2D Networks via the Thiol-Epoxide Reaction on 1T/2H MoS_2 Polytypes. *Mater. Chem. Front.* **2021**, *5*, 3470−3479.

(8) Knirsch, K. C.; Berner, N. C.; Nerl, H. C.; Cucinotta, C. S.; Gholamvand, Z.; McEvoy, N.; Wang, Z.; Abramovic, I.; Vecera, P.; Halik, M.; Sanvito, S.; Duesberg, G. S.; Nicolosi, V.; Hauke, F.; Hirsch, A.; Coleman, J. N.; Backes, C. Basal-Plane Functionalization of Chemically Exfoliated Molybdenum Disulfide by Diazonium Salts. *ACS Nano* **2015**, *9*, 6018−6030.

(9) Tuci, G.; Mosconi, D.; Rossin, A.; Luconi, L.; Agnoli, S.; Righetto, M.; Pham-Huu, C.; Ba, H.; Cicchi, S.; Granozzi, G.; Giambastiani, G. Surface Engineering of Chemically Exfoliated MoS_2 in a "Click": How To Generate Versatile Multifunctional Transition Metal Dichalcogenides-Based Platforms. *Chem. Mater.* **2018**, *30*, 8257−8269.
(10) Smith, R. J.; King, P. J.; Lotya, M.; Wirtz, C.; Khan, U.; De, S.; O'Neill, A.; Duesberg, G. S.; Grunlan, J. C.; Moriarty, G.; Chen, J.; Wang, J.; Minett, A. I.; Nicolosi, V.; Coleman, J. N. Large-Scale Exfoliation of Inorganic Layered Compounds in Aqueous Surfactant Solutions. *Adv. Mater.* **2011**, *23*, 3944−3948.
(11) Halim, U.; Zheng, C. R.; Chen, Y.; Lin, Z.; Jiang, S.; Cheng, R.; Huang, Y.; Duan, X. A Rational Design of Cosolvent Exfoliation of Layered Materials by Directly Probing Liquid−Solid Interaction. *Nat. Commun.* **2013**, *4*, 2213.
(12) Coleman, J. N.; Lotya, M.; O'Neill, A.; Bergin, S. D.; King, P. J.; Khan, U.; Young, K.; Gaucher, A.; De, S.; Smith, R. J.; Shvets, I. V.; Arora, S. K.; Stanton, G.; Kim, H.-Y.; Lee, K.; Kim, G. T.; Duesberg, G. S.; Hallam, T.; Boland, J. J.; Wang, J. J.; et al. Two-Dimensional Nanosheets Produced by Liquid Exfoliation of Layered Materials. *Science* **2011**, *331*, 568−571.
(13) Chen, X.; Berner, N. C.; Backes, C.; Duesberg, G. S.; McDonald, A. R. Functionalization of Two-Dimensional MoS_2: On the Reaction Between MoS_2 and Organic Thiols. *Angew. Chem., Int. Ed.* **2016**, *55*, 5803−5808.
(14) Jawaid, A.; Nepal, D.; Park, K.; Jespersen, M.; Qualley, A.; Mirau, P.; Drummy, L. F.; Vaia, R. A. Mechanism for Liquid Phase Exfoliation of MoS_2. *Chem. Mater.* **2016**, *28*, 337−348.
(15) Jawaid, A. M.; Ritter, A. J.; Vaia, R. A. Mechanism for Redox Exfoliation of Layered Transition Metal Dichalcogenides. *Chem. Mater.* **2020**, *32*, 6550−6565.
(16) Jawaid, A.; Che, J.; Drummy, L. F.; Bultman, J.; Waite, A.; Hsiao, M.-S.; Vaia, R. A. Redox Exfoliation of Layered Transition Metal Dichalcogenides. *ACS Nano* **2017**, *11*, 635−646.
(17) Vera-Hidalgo, M.; Giovanelli, E.; Navío, C.; Pérez, E. M. Mild Covalent Functionalization of Transition Metal Dichalcogenides with Maleimides: A "Click" Reaction for 2H-MoS_2 and WS_2. *J. Am. Chem. Soc.* **2019**, *141*, 3767−3771.
(18) Quirós-Ovies, R.; Vázquez Sulleiro, M.; Vera-Hidalgo, M.; Prieto, J.; Gómez, I. J.; Sebastián, V.; Santamaría, J.; Pérez, E. M. Controlled Covalent Functionalization of 2 H-MoS_2 with Molecular or Polymeric Adlayers. *Chem.—Eur. J.* **2020**, *26*, 6629−6634.
(19) Vishnoi, P.; Sampath, A.; Waghmare, U. V.; Rao, C. N. R. Covalent Functionalization of Nanosheets of MoS_2 and $MoSe_2$ by Substituted Benzenes and Other Organic Molecules. *Chem.—Eur. J.* **2017**, *23*, 886−895.
(20) Krajewska, A. M.; Paiva, A. E.; Morris, M.; McDonald, A. R. Reduction of Exfoliated MoS_2 Nanosheets Yields the Semi-Conducting 2H-Polymorph Rather Than the Metallic 1T-Polymorph. *Eur. J. Inorg. Chem.* **2024**, *27*, No. e202400292.
(21) Wang, C.; He, Q.; Halim, U.; Liu, Y.; Zhu, E.; Lin, Z.; Xiao, H.; Duan, X.; Feng, Z.; Cheng, R.; Weiss, N. O.; Ye, G.; Huang, Y.-C.; Wu, H.; Cheng, H.-C.; Shakir, I.; Liao, L.; Chen, X.; Goddard III, W. A.; Huang, Y.; Duan, X. Monolayer Atomic Crystal Molecular Superlattices. *Nature* **2018**, *555*, 231−236.
(22) Jawaid, A.; Pike, N. A.; Pachter, R.; Vaia, R. Basal Surface Hybridization of Group V Layered Transition Metal Dichalcogenides. *ACS Mater. Au* **2023**, *3*, 55−65.
(23) Dasgupta, A.; López-Arteaga, R.; Park, H. Y.; Kerwin, B. P.; Utama, M. I. B.; Sadhukhan, T.; Gavin, S. C.; Wan, X.; Kachman, D. E.; Wang, W.; Ananth, R.; Vong, A. F.; Stern, N. P.; Schatz, G. C.; Ma, X.; Marks, T. J.; Weiss, E. A.; Hersam, M. C. Carbene Functionalization of Monolayer Tungsten Disulfide for Enhanced Quantum Emission. *ACS Nano* **2025**, *19*, 21844−21857.
(24) Choi, Y.; Park, C. S.; Tran, H.-V.; Li, C.-H.; Crudden, C. M.; Lee, T. R. Functionalized N-Heterocyclic Carbene Monolayers on Gold for Surface-Initiated Polymerizations. *ACS Appl. Mater. Interfaces* **2022**, *14*, 44969−44980.
(25) Chalmpes, N.; Susner, M. A.; Velez, M.; Alsmaeil, A. W.; Jawaid, A.; Vaia, R. A.; Giannelis, E. P. Enhanced Yield and Compatibility of Exfoliated MoS_2 through Iodine-Assisted Thermal Treatment of Powders. *Adv. Funct. Mater.* **2025**, *35*, 2420741.
(26) Busch, R. T.; Sun, L.; Austin, D.; Jiang, J.; Miesle, P.; Susner, M. A.; Conner, B. S.; Jawaid, A.; Becks, S. T.; Mahalingam, K.; Velez, M. A.; Torsi, R.; Robinson, J. A.; Rao, R.; Glavin, N. R.; Vaia, R. A.; Pachter, R.; Joshua Kennedy, W.; Vernon, J. P.; Stevenson, P. R. Exfoliation Procedure-Dependent Optical Properties of Solution Deposited MoS_2 Films. *npj 2D Mater. Appl.* **2023**, *7*, 12.
(27) Backes, C.; Smith, R. J.; McEvoy, N.; Berner, N. C.; McCloskey, D.; Nerl, H. C.; O'Neill, A.; King, P. J.; Higgins, T.; Hanlon, D.; Scheuschner, N.; Maultzsch, J.; Houben, L.; Duesberg, G. S.; Donegan, J. F.; Nicolosi, V.; Coleman, J. N. Edge and Confinement Effects Allow in Situ Measurement of Size and Thickness of Liquid-Exfoliated Nanosheets. *Nat. Commun.* **2014**, *5*, 4576.
(28) Nguyen, T. P.; Sohn, W.; Oh, J. H.; Jang, H. W.; Kim, S. Y. Size-Dependent Properties of Two-Dimensional MoS_2 and WS_2. *J. Phys. Chem. C* **2016**, *120*, 10078−10085.
(29) Tongay, S.; Zhou, J.; Ataca, C.; Liu, J.; Kang, J. S.; Matthews, T. S.; You, L.; Li, J.; Grossman, J. C.; Wu, J. Broad-Range Modulation of Light Emission in Two-Dimensional Semiconductors by Molecular Physisorption Gating. *Nano Lett.* **2013**, *13*, 2831−2836.
(30) Vaia, R. A.; Teukolsky, R. K.; Giannelis, E. P. Interlayer Structure and Molecular Environment of Alkylammonium Layered Silicates. *Chem. Mater.* **1994**, *6*, 1017−1022.
(31) Machado, Y. D. R.; Prando, G. A.; Araújo, L. F.; da Silva, L. V.; Salles, M. O.; Grasseschi, D.; Margulis, W.; Chalmpes, N.; Vaia, R. A.; Gomes, A. S. L.; Carvalho, I. C. S. Electric-Field-Induced Instability of Redox-Exfoliated Layered Transition Metal Dichalcogenides. *J. Phys. Chem. C* **2025**, *129*, 2582−2589.
(32) Zhou, J.; Ren, H.; Zhou, J.; Wan, Z.; Qian, Q.; Peng, B.; Du, S.; Yan, X.; Pan, X.; Sofer, Z.; Zhang, A.; Huang, Y.; Duan, X. Modular Assembly of a Library of Hybrid Superlattices and Artificial Quantum Solids. *Matter* **2024**, *7*, 1131−1145.
(33) Lockhart de la Rosa, C. J.; Phillipson, R.; Teyssandier, J.; Adisoejoso, J.; Balaji, Y.; Huyghebaert, C.; Radu, I.; Heyns, M.; De Feyter, S.; De Gendt, S. Molecular Doping of MoS_2 Transistors by Self-Assembled Oleylamine Networks. *Appl. Phys. Lett.* **2016**, *109*, 253112.
(34) Yang, R.; Mei, L.; Zhang, Q.; Fan, Y.; Shin, H. S.; Voiry, D.; Zeng, Z. High-Yield Production of Mono- or Few-Layer Transition Metal Dichalcogenide Nanosheets by an Electrochemical Lithium Ion Intercalation-Based Exfoliation Method. *Nat. Protoc.* **2022**, *17*, 358−377.
(35) Fan, X.; Xu, P.; Li, Y. C.; Zhou, D.; Sun, Y.; Nguyen, M. A. T.; Terrones, M.; Mallouk, T. E. Controlled Exfoliation of MoS_2 Crystals into Trilayer Nanosheets. *J. Am. Chem. Soc.* **2016**, *138*, 5143−5149.
(36) Ries, L.; Petit, E.; Michel, T.; Diogo, C. C.; Gervais, C.; Salameh, C.; Bechelany, M.; Balme, S.; Miele, P.; Onofrio, N.; Voiry, D. Enhanced Sieving from Exfoliated MoS_2 Membranes via Covalent Functionalization. *Nat. Mater.* **2019**, *18*, 1112−1117.
(37) Li, H.; Zhang, Q.; Yap, C. C. R.; Tay, B. K.; Edwin, T. H. T.; Olivier, A.; Baillargeat, D. From Bulk to Monolayer MoS_2: Evolution of Raman Scattering. *Adv. Funct. Mater.* **2012**, *22*, 1385−1390.
(38) Conley, H. J.; Wang, B.; Ziegler, J. I.; Haglund, R. F., Jr.; Pantelides, S. T.; Bolotin, K. I. Bandgap Engineering of Strained Monolayer and Bilayer MoS_2. *Nano Lett.* **2013**, *13*, 3626−3630.
(39) Chakraborty, B.; Bera, A.; Muthu, D. V. S.; Bhowmick, S.; Waghmare, U. V.; Sood, A. K. Symmetry-Dependent Phonon Renormalization in Monolayer MoS_2 Transistor. *Phys. Rev. B: Condens. Matter Mater. Phys.* **2012**, *85*, 161403.
(40) Sun, Y.; Yin, S.; Peng, R.; Liang, J.; Cong, X.; Li, Y.; Li, C.; Wang, B.; Lin, M.-L.; Tan, P.-H.; Wan, C.; Liu, K. Abnormal Out-of-Plane Vibrational Raman Mode in Electrochemically Intercalated Multilayer MoS_2. *Nano Lett.* **2023**, *23*, 5342−5349.
(41) He, K.; Poole, C.; Mak, K. F.; Shan, J. Experimental Demonstration of Continuous Electronic Structure Tuning via Strain in Atomically Thin MoS_2. *Nano Lett.* **2013**, *13*, 2931−2936.
(42) Lloyd, D.; Liu, X.; Christopher, J. W.; Cantley, L.; Wadehra, A.; Kim, B. L.; Goldberg, B. B.; Swan, A. K.; Bunch, J. S. Band Gap

https://doi.org/10.1021/acsanm.5c04402
ACS Appl. Nano Mater. 2025, 8, 22400−22417

Engineering with Ultralarge Biaxial Strains in Suspended Monolayer MoS_2. *Nano Lett.* **2016**, *16*, 5836−5841.
(43) Zhang, S.; Hill, H. M.; Moudgil, K.; Richter, C. A.; Hight Walker, A. R.; Barlow, S.; Marder, S. R.; Hacker, C. A.; Pookpanratana, S. J. C. Controllable, Wide-Ranging n-Doping and p-Doping of Monolayer Group 6 Transition-Metal Disulfides and Diselenides. *Adv. Mater.* **2018**, *30*, 1802991.
(44) Michail, A.; Delikoukos, N.; Parthenios, J.; Galiotis, C.; Papagelis, K. Optical Detection of Strain and Doping Inhomogeneities in Single Layer MoS_2. *Appl. Phys. Lett.* **2016**, *108*, 173102.
(45) Kolhe, P. T.; Thorat, A. B.; Phatangare, A. B.; Jadhav, P. R.; Dalvi, S. N.; Dhole, S. D.; Dahiwale, S. S. Strain Induced Study on MoS_2 Thin Films Due to Ion and Gamma Irradiation. *J. Alloys Compd.* **2022**, *896*, 162969.
(46) He, Q.; Lin, Z.; Ding, M.; Yin, A.; Halim, U.; Wang, C.; Liu, Y.; Cheng, H.-C.; Huang, Y.; Duan, X. In Situ Probing Molecular Intercalation in Two-Dimensional Layered Semiconductors. *Nano Lett.* **2019**, *19*, 6819−6826.
(47) Splendiani, A.; Sun, L.; Zhang, Y.; Li, T.; Kim, J.; Chim, C.-Y.; Galli, G.; Wang, F. Emerging Photoluminescence in Monolayer MoS_2. *Nano Lett.* **2010**, *10*, 1271−1275.
(48) Scheuschner, N.; Ochedowski, O.; Kaulitz, A.-M.; Gillen, R.; Schleberger, M.; Maultzsch, J. Photoluminescence of Freestanding Single- and Few-Layer MoS_2. *Phys. Rev. B: Condens. Matter Mater. Phys.* **2014**, *89*, 125406.
(49) Mak, K. F.; He, K.; Lee, C.; Lee, G. H.; Hone, J.; Heinz, T. F.; Shan, J. Tightly Bound Trions in Monolayer MoS_2. *Nat. Mater.* **2013**, *12*, 207−211.
(50) Rosenberger, M. R.; Chuang, H.-J.; McCreary, K. M.; Li, C. H.; Jonker, B. T. Electrical Characterization of Discrete Defects and Impact of Defect Density on Photoluminescence in Monolayer WS_2. *ACS Nano* **2018**, *12*, 1793−1800.
(51) Chow, P. K.; Jacobs-Gedrim, R. B.; Gao, J.; Lu, T.-M.; Yu, B.; Terrones, H.; Koratkar, N. Defect-Induced Photoluminescence in Monolayer Semiconducting Transition Metal Dichalcogenides. *ACS Nano* **2015**, *9*, 1520−1527.
(52) Yan, E. X.; Cabán-Acevedo, M.; Papadantonakis, K. M.; Brunschwig, B. S.; Lewis, N. S. Reductant-Activated, High-Coverage, Covalent Functionalization of 1T′-MoS_2. *ACS Mater. Lett.* **2020**, *2*, 133−139.
(53) Jiménez Sandoval, S.; Yang, D.; Frindt, R. F.; Irwin, J. C. Raman Study and Lattice Dynamics of Single Molecular Layers of MoS_2. *Phys. Rev. B: Condens. Matter Mater. Phys.* **1991**, *44*, 3955−3962.
(54) Heising, J.; Kanatzidis, M. G. Exfoliated and Restacked MoS_2 and WS_2: Ionic or Neutral Species? Encapsulation and Ordering of Hard Electropositive Cations. *J. Am. Chem. Soc.* **1999**, *121*, 11720−11732.
(55) Tang, Q.; Jiang, D. Stabilization and Band-Gap Tuning of the 1T-MoS_2 Monolayer by Covalent Functionalization. *Chem. Mater.* **2015**, *27*, 3743−3748.
(56) Ott, L. S.; Cline, M. L.; Deetlefs, M.; Seddon, K. R.; Finke, R. G. Nanoclusters in Ionic Liquids: Evidence for N-Heterocyclic Carbene Formation from Imidazolium-Based Ionic Liquids Detected by 2H NMR. *J. Am. Chem. Soc.* **2005**, *127*, 5758−5759.
(57) Fèvre, M.; Pinaud, J.; Leteneur, A.; Gnanou, Y.; Vignolle, J.; Taton, D.; Miqueu, K.; Sotiropoulos, J.-M. Imidazol(in)Ium Hydrogen Carbonates as a Genuine Source of N-Heterocyclic Carbenes (NHCs): Applications to the Facile Preparation of NHC Metal Complexes and to NHC-Organocatalyzed Molecular and Macromolecular Syntheses. *J. Am. Chem. Soc.* **2012**, *134*, 6776−6784.
(58) Dupont, J.; Spencer, J. On the Noninnocent Nature of 1,3-Dialkylimidazolium Ionic Liquids. *Angew. Chem., Int. Ed.* **2004**, *43*, 5296−5297.
(59) Daud, N. M. a. N.; Bakis, E.; Hallett, J. P.; Weber, C. C.; Welton, T. Evidence for the Spontaneous Formation of N-Heterocyclic Carbenes in Imidazolium Based Ionic Liquids. *Chem. Commun.* **2017**, *53*, 11154−11156.
(60) Crudden, C. M.; Horton, J. H.; Narouz, M. R.; Li, Z.; Smith, C. A.; Munro, K.; Baddeley, C. J.; Larrea, C. R.; Drevniok, B.; Thanabalasingam, B.; McLean, A. B.; Zenkina, O. V.; Ebralidze, I. I.; She, Z.; Kraatz, H.-B.; Mosey, N. J.; Saunders, L. N.; Yagi, A. Simple Direct Formation of Self-Assembled N-Heterocyclic Carbene Monolayers on Gold and Their Application in Biosensing. *Nat. Commun.* **2016**, *7*, 12654.
(61) Amyes, T. L.; Diver, S. T.; Richard, J. P.; Rivas, F. M.; Toth, K. Formation and Stability of N-Heterocyclic Carbenes in Water: The Carbon Acid pKa of Imidazolium Cations in Aqueous Solution. *J. Am. Chem. Soc.* **2004**, *126*, 4366−4374.
(62) Henrique Teles, J.; Melder, J.-P.; Ebel, K.; Schneider, R.; Gehrer, E.; Harder, W.; Brode, S.; Enders, D.; Breuer, K.; Raabe, G. The Chemistry of Stable Carbenes. Part 2. Benzoin-Type Condensations of Formaldehyde Catalyzed by Stable Carbenes. *Helv. Chim. Acta* **1996**, *79*, 61−83.
(63) Jones, L. O.; Sadhukhan, T.; Schatz, G. C. Localized π Surface States on 2D Molybdenum Disulfide from Carbene-Functionalization as a Qubit Design Strategy. *ACS Phys. Chem. Au* **2022**, *2*, 277−281.
(64) Sadhukhan, T.; Schatz, G. C. Generating Bright Emissive States by Modulating the Bandgap of Monolayer Tungsten Diselenide. *J. Phys. Chem. C* **2022**, *126*, 5598−5606.
(65) Gao, J.; Li, N.; Dai, B.; Yu, W.; Zhou, X.; Chen, C.; Fujisawa, K.; Yang, Z.; Dai, S.; Sun, Y. N-Heterocyclic Carbene Functionalization of 2D Transition Metal Dichalcogenides via a Frustrated Lewis Pair Strategy. *Adv. Funct. Mater.* **2025**, 2502325.
(66) Schöllhorn, R. 10—Solvated Intercalation Compounds of Layered Chalcogenide and Oxide Bronzes. In *Intercalation Chemistry*; Whittingham, M. S., Jacobson, A. J., Eds.; Academic Press, 1982; pp 315−360.
(67) Hollóczki, O.; Gerhard, D.; Massone, K.; Szarvas, L.; Németh, B.; Veszprémi, T.; Nyulászi, L. Carbenes in Ionic Liquids. *New J. Chem.* **2010**, *34*, 3004−3009.
(68) Wild, M.; Stolz, F.; Naumov, S.; Abel, B. On the in Situ Formation of Carbenes in Ionic Liquids. *Mol. Phys.* **2021**, *119*, No. e1974589.
(69) Amsterdam, S. H.; Marks, T. J.; Hersam, M. C. Leveraging Molecular Properties to Tailor Mixed-Dimensional Heterostructures beyond Energy Level Alignment. *J. Phys. Chem. Lett.* **2021**, *12*, 4543−4557.
(70) Backes, C.; Hanlon, D.; Szydlowska, B. M.; Harvey, A.; Smith, R. J.; Higgins, T. M.; Coleman, J. N. Preparation of Liquid-Exfoliated Transition Metal Dichalcogenide Nanosheets with Controlled Size and Thickness: A State of the Art Protocol. *J. Vis. Exp.* **2016**, No. e54806.

https://doi.org/10.1021/acsanm.5c04402
ACS Appl. Nano Mater. 2025, 8, 22400−22417